

# Scanning Probe Microscopy in Practical Diagnostic: 3D Topography Imaging and Nanometrology

Petro M. Lytvyn

**Abstract** This overview presents a common approach of practical atomic force microscopy (AFM) diagnostic of surfaces at the sub-micrometer and nano-meter levels. A common metrological model of AFM and sources of uncertainty of measurements are analyzed. Procedures for scanner and tip calibration are presented. Application of precise topometry concerning geometrical sizes of surface features and its metrological traceability are illustrated using original data of systematic AFM diagnostics applied to semiconductor nano-structures with quantum dots grown by molecular beam epitaxy. A number of weighty results important to understand physics of processes during structural ordering in low-dimensional semiconductor systems has been described. Physical, methodological and experimental parts have been presented without extended details that could be found in the complete list of references.

## 1 Introduction

In actual scientific and technological investigations, methods of scanning probe microscopy (SPM) comprise one of the advanced positions. For several decades of its existence, SPM was developed as a separate area of scientific and engineering explorations. Realized for the first time by IBM collaborators in 1981, the tunnel microscope [1–3] became the father of a new generation of microscopes based on the idea of local diagnostics of surface properties by using the probe body (probe, sensor) with the size of operation area (tip) close to several unities or tens of nanometer.

---

P.M. Lytvyn (✉)

V. Lashkarev Institute of Semiconductor Physics, National Academy of Sciences of Ukraine, 41, Nauky Pr, Kyiv 03028, Ukraine  
e-mail: plyt@isp.kiev.ua; peter.lytvyn.isp@gmail.com

From the historical viewpoint, the principal ideas of scanning probe microscopy can be dated back to 1928, when E. H. Synge proposed a theoretical approach to overcome the diffraction limit in conventional optical microscopy. Scanning with a small nanoscale probe (sub-wavelength aperture) over a sample in proximity to its surface was suggested. The idea to use tunneling current to control stylus-surface distance was described by Russell Young in 1966 [4]. The first instrument, where the probe scanned over surface and measured height of single atomic steps using tunneling current was introduced by his scientific group in 1971 [5]. Ten years later, group of Binnig (Nobel Prize in 1986) demonstrated first surface image with atomic resolution obtained by STM [3]. Then, Binnig et al. realized the scanning probe microscope operating due to local force interaction in 1986 [6, 7].

In a general case, current scanning probe microscopes are high-tech diagnostic facilities combining in one device the whole complex of means for performing surface diagnostics. As a rule, these methods are based on physical effects of electric and force interaction between the probe and surface. The above mentioned scanning tunnel microscopy (STM), atomic force microscopy (AFM) and its derivatives: electrostatic force microscopy (EFM) [8, 9], scanning force Kelvin-probe microscopy (SFKPM) [10, 11], magnetic force microscopy (MFM) [12] are related to these methods. Also widely used are SPM methods for local diagnostics of surface electrical properties where the AFM method provides control of force interaction “probe—surface” as well as mapping the relief, while independent channels of measurements register current flow (conductive atomic force microscopy [13, 14]), local resistance (scanning spreading resistance microscopy [15]) or the capacitance “probe—surface” (scanning capacitance microscopy [16]).

In addition to mapping the surface properties, the above methods allow for obtaining respective spectroscopic data in a chosen point. For example, atomic force spectroscopy (that enables to measure the dependence of the interaction force on the distance probe—surface) possesses a sufficient range of sensitivity to obtain important information on specificity of intermolecular interaction [17, 18], on the one hand, and perform nanomechanical investigations of local surface properties [19], on the other hand. In their turn, conducting AFM and EFM allow obtaining the current-voltage and capacitance-voltage characteristics of surfaces with a high spatial resolution (area of the contact is close to 10–100 nm<sup>2</sup>) [20–22]. Besides, most of the series SPM models are rather efficiently used in intentional modification of a surface in nano-probe lithography, manipulation and preparation of nano-objects [23, 24].

A cogent advantage of SPM is its capability to obtain reliable data about surface micro- or nano-relief both in vacuum and in ambient atmosphere as well as in liquid medium. The objects of investigations do not require any special preparation as it takes place in some other methods. It is natural that preparation of the samples is an important stage of SPM diagnostics, but in this case it is directed not to modification of the object, which provides usability of this diagnostic method, but to provide specific conditions for measuring the necessary properties. For example, it is essential to remove random contaminations and adsorbent layer from nano-structured surface before mapping their surface or application of more complex

protocols for preparation of biological objects, namely: separation, extraction, immobilization on the substrate and functionalization of the AFM probe tip. Due to the extremely wide spectrum of diagnostic methods, SPM is efficiently used in various scientific and technical areas, starting from fundamental investigations in physics of surfaces, applied materials science, diagnostic of functional elements in nano-electronic devices, and up to nano-medicine and biosensor technologies.

Particularity of SPM application sets respective requirements on the way of their hardware realization. Fundamental investigations at the atomic level require ultrahigh-vacuum systems providing purity and stability of the studied surface as well as high sensitivity and speed of measurements. For solving most of tasks in applied diagnostics of surfaces at micro- and nano-levels, SPM methods operating in air and liquid media and possessing the field of view up to  $100 \times 100 \mu\text{m}^2$  are the most suitable. In biomedical investigations, the main priority in the SPM construction is the possibility to perform measurements in various liquid media as close as possible to the native ones and convenience to operate with biomaterials.

However, despite relative simplicity in performing SPM investigations, obtaining reliable data and their scientific interpretation require understanding of physical processes of probe-surface interaction, knowledge on how one should separate head and minor factors that influence formation of SPM images in dependence of measurement conditions. Not less important component is metrological aspects of SPM diagnostics. Here, main questions are those concerning calibration of scanners, shape of the probe tip, determination of mechanical parameters describing cantilevers in measurements based on the AFM method, usage of respective test structures in electric-force and capacitance measurements.

Despite the fact that SPM is one of the most simple and convenient tools for obtaining quantitative topographical data in the micro- and nano-scale range and providing better accuracy than other microscopic techniques, determination of other exact quantitative surface parameters (chemical, mechanical, magnetic, electrical) is mated with considerable methodical difficulties. In most of these cases, SPM is used for qualitative and semi-quantitative estimation, and currently is not recommended for metrological purposes. However, even rude SPM measurements and mapping the above parameters are of a great scientific and applied interest. Besides, hardware and methodical bases in SPM are continuously perfected, which constantly lowers uncertainties in measurements.

A lot of monographs and informative reviews are devoted to generalization and systematization of theoretical approaches in considering the features of probe-surface interaction in diversity of SPM methods as well as methodical and applied SPM aspects of diagnostics. However, there is a lack of examples of application of systems approach in solution of diagnostical tasks, which could combine various methodical and analytical approaches with account of metrological peculiarities inherent to SPM diagnostics. We hope that description of our own experience concerning complex application of SPM diagnostics in a number of applied tasks, peculiarities of performing measurements and interpretation of the data obtained will be useful both for specialists and beginners in this field.

## 2 Atomic Force Microscopy and Spectroscopy

### 2.1 Atomic Force Microscopy: Physical Principles and Technical Realization

Let us remind the basic principles of functioning and hardware realization of the scanning atomic force microscopy, as this method is most often used in diagnostic of functional materials and device structures. The AFM method is based on one of the most universal interactions in nature—attraction and repulsion between bodies. The basic set-up of the modern SPM for scientific and applied investigations can be represented by the following components (Fig. 1): tip, scanner for displacement of the tip, system for registration of parameters corresponding to tip-surface interaction and the feedback loop, console for control and visualization of measurement results, system for vibration and noise isolation.

In the atomic force microscope, a special monitoring system performs precise raster displacement of solid probe (micromachine in the form of tip with the radius of 5–30 nm that is fixed to elastic cantilever) above the studied surface. The force of probe-surface interaction is kept constant due to changing the probe height above the surface. Values of voltages on piezoelements of the three-coordinate displacement system (scanner), by using preliminary calibration, are converted by AFM software into 3D map of the surface.

Bearing in mind the way providing force interaction probe-surface, the modes of AFM operation can be separated by three groups, namely: continuous contact, periodical contact (“intermittent contact mode”) and noncontact ones. Latter two modes use modulation methods, where the probe vibrates with the frequency of its mechanical resonance (or near it) and changes in amplitude, frequency or phase inherent to these vibrations are monitored in the feedback loop. These methods are also named the dynamical ones. When mapping a relief in the contact mode, it is important to keep the constant value of the probe cantilever deflection, which corresponds to the state of equilibrium of all the forces acting on the probe from the surface and the force caused by elastic deformation of the cantilever. Measurements of absolute deflection values are not necessary when mapping the surface. By analogy, in the other modes one should monitor only changes in the vibration amplitude or shift of phase/frequency in topometric measurements.

However measurements of the absolute value for the deflection of the probe cantilever are important in force spectroscopic investigations. If sensitivity of the measuring system to probe deformation, cantilever spring constant and the vertical scanner translation are known, one can obtain quantitative dependence of the force value for probe-surface interaction on the distance. A typical measurements scheme and the force-distance curve are shown in Fig. 2. In the position I, the probe is far from surface, and interaction between them is missed. In the position II, the probe is approached to the surface so close (movement along a curve is indicated by arrow), that jumps to contact with the surface due to action of van der Waals attraction forces. Thus, if the measurement takes place in air, the layer of

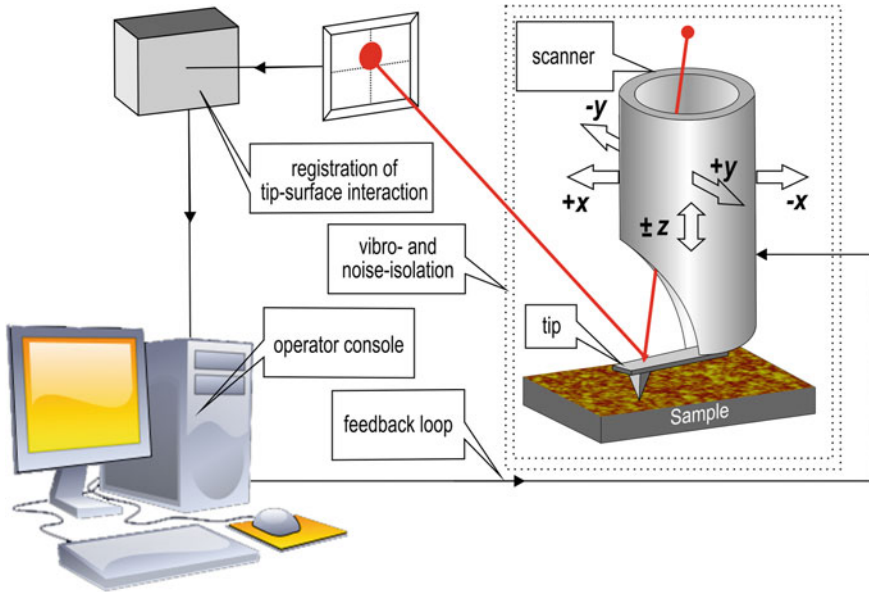


**Fig. 1** General functional setup of a scanning probe microscope

liquid condensed on the surface can play a significant role. In the position III, the probe reaches the given maximum of the repulsion force and is withdrawn from the surface. Hysteresis occurs due to adhesive attraction forces. In the position IV, the elastic deformation force of deflected cantilever exceeds the adhesive force and probe released by surface. In the position V, the AFM probe cantilever returns to the equilibrium state.

In terms of distance, we have the following situation. When the AFM probe approaches to surface, it begins to perceive long-range electrostatic and magnetic interactions starting from the distance close to 1 μm. At the distances of 10–100 nm, the main force interactions will be long-range van der Waals interactions. Even closer, in ambient conditions, water bridges can appear between tip apex and surface due to capillary condensation. Charge transfer via tunneling appears, and van der Waals forces become dominant at the distances of 1–10 nm. At contact, the Coulomb repulsion takes place. Deformation of AFM tip or sample can occur at high values of applied forces.

There are various physical models describing tip-surface interaction depending on acting forces [25, 26]. The simplest model for an interatomic force that covers both the short range repulsive and long-range attractive interactions is based on the Lennard-Jones (LJ) potential. It can be described by the following formula:

$$V = 4\varepsilon \left[ \left( \frac{\sigma}{r} \right)^{12} - \left( \frac{\sigma}{r} \right)^6 \right]$$

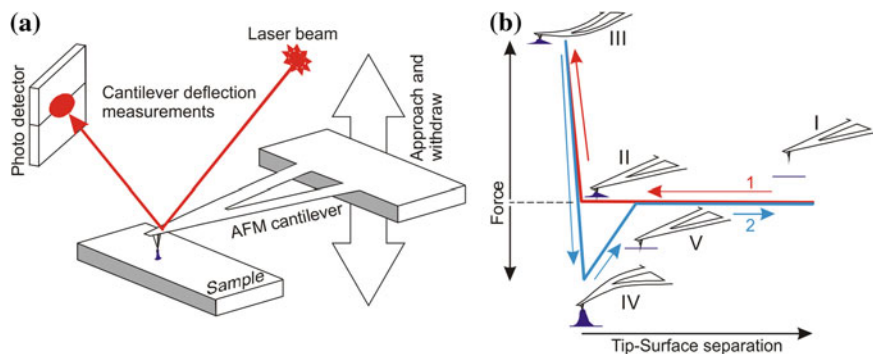
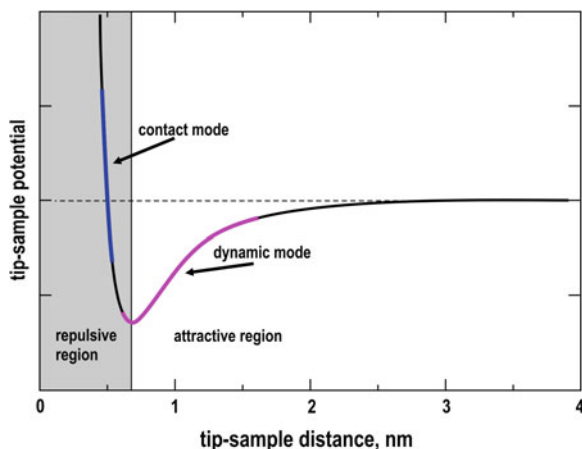


**Fig. 2** Scheme of measurements (a) and schematic view of force curves when measuring in air (b): approaching curve (1), withdrawing curve (2)

**Fig. 3** Typical tip-sample interaction potential dependence on distance with marked regions of contact and non-contact mode performance



where  $\varepsilon$  corresponds to the depth of the potential well (reflected interaction strength) and  $\sigma$  is the interatomic distance where the potential is zero,  $r$  is an interatomic distance for a system of two LJ particles. Schematically, the dependence of the LJ potential on the tip-sample distance is shown in Fig. 3. Marked in the figure are areas where contact and dynamic AFM modes are realized.

A good starting point to understand force curves can be found in B. Cappella review [27]. The raw AFM measured force curve does not reproduce a clear tip-surface interaction forces. The sum of interaction forces  $F(D)$ , elastic force of cantilever and its deflection are hidden in the force-displacement data. Besides, in the vicinity of the extreme observed for the  $F(D)$  function, there exists an ambiguity leading to difference between curves of approaching the probe to and removing it from the surface. Figure 4 shows the dependence of the interatomic

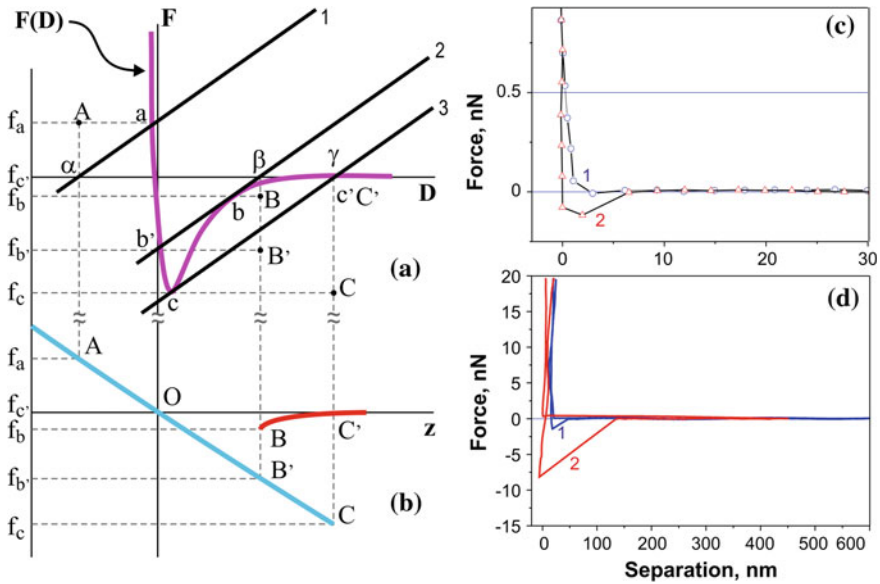


**Fig. 4** Construction of experimental force-distance curve. Dependence of the Lenard-Jones force on distance (a, curve) and the force of elastic deformation of tip cantilever (a, lines 1, 2, 3). The respective curve measured with AFM (b). Experimental force—tip surface separation curves (d) recorded in air (1) and under water buffer (2). Jump-to-contact of corresponding curves shown in (c)

Lennard-Jones force on the distance [27]. In these coordinates, the force of tip cantilever elastic deformation is represented with a straight line with the slope equal to the cantilevers spring constant in accord with Hooke’s law. The force of tip-surface interaction is balanced by the force of cantilever elastic deformation in every point of the force curve that corresponds, for example, the intersection points in the  $F(D)$  dependence and straight lines 1, 2 and 3. It is seen that moving the straight line from the right to the left (curve of approaching), in the region between  $c'$  and  $b'$  (Fig. 4a) we obtain three intersections and hence three equilibrium positions. Two of these positions (between  $c'$  and  $b$  and between  $c$  and  $b'$ ) are stable, while the third position (between  $b$  and  $c$ ) is unstable because of two possible points of balance. At the stage of approaching, the tip follows the trajectory from  $c'$  to  $b$  and then “jumps” from  $b$  to  $b'$  (i.e., from the force value  $f_b$  to  $f_{b'}$ ). During retraction, the tip follows the trajectory from  $b'$  to  $c$  and then jumps from  $c$  to  $c'$  (i.e., from  $f_c$  to  $f_{c'}$ ).

These jumps correspond to the discontinuities  $BB'$  and  $CC'$  in the Fig. 4b. Thus, the region between  $b$  and  $c$  is not measured. The difference in path between approach and withdrawal curves is usually called “force—displacement curve hysteresis”. The two discontinuities in force values are called “jump-to-contact” in the approach curve ( $BB'$ ) and “jump-off-contact” in the withdrawal curve ( $CC'$ ).

Caused by the above reasons, the force curve measured with the microscope has the look shown in Fig. 4c, d. The ambiguity in the vicinity of CB points can be avoided by increasing the stiffness of the probe cantilever. However, on the other hand, it will cause a loss in sensitivity. Therefore, the choice of elastic parameters inherent to the cantilever depends on peculiarities of the solved task. It is noteworthy that for most of routine spectroscopic AFM measurements minimization of “jump-to-contact” and “jump-off-contact” effects is not critical. Curves bring sufficient information to recover parameters of real probe-surface interaction after separation of the probe elastic component. Besides, as seen from Fig. 3, dynamic AFM methods operate in the very “problem” range. In these modulation methods, they use more complex models to analyze the obtained data [28, 29].

## ***2.2 Atomic Force Microscopy 3D Metrology for Assessment Surface Topography***

From the viewpoint of using SPM for maintenance of up-to-date nanotechnologies, metrological traceability of measurements is very important [30–33]. Although, nanotechnology now should be understood as science and technology of the structures, in which sizes of separate elements lie within the range 0.1–100 nm, nanometrology essentially covers this diapason. Measurements should be performed with the accuracy lying inside this or less dimensional diapason. To solve these tasks, scanning probe microscopes are ideal candidates that are capable to provide 3D-measurements of geometrical sizes and diverse physical and chemical properties of objects in the dimensional scale from parts of angstroms up to hundreds of micrometers.

On the one hand, flexibility and multipurpose character of SPM methods provides their wide application in various fields of science and technique (materials science, electronics, optics, energetic, food industry, biology, pharmacology, medicine, etc.), but on the other hand, it awfully complicates development of joint standards for SPM measurements. Probe microscopy of various purposes essentially differs by its hardware realization, list and level of fulfilling the measurement methods, analytical software, and so on.

However, to verify and calibrate SPMs, one should use common unified approaches that could provide worldwide comparability of measurement results and metrological traceability. The most accepted instructions are usually documentary standards developed in committees of the International Standardization Organization ISO. The ISO committee in charge of drafting standards for SPM is the Technical Committee ISO/TC 201 Surface Chemical Analysis, mainly its subcommittee SC 9 Scanning Probe Microscopies established in 2004. Up to date, about a dozen of normative documents are under development, with the first ones already published or nearing completion [34].



Standards regulate both using the respective terminology and set procedures for testing the microscope units as well as parameters of probes. Developed in addition are also the standards that regulate usage of separate methods for SPM measurements (see, for instance [35]). Beside these standards, important are those that regulate determination of respective quantitative characteristics by the data of SPM measurements. First positions in the list of these standards can be occupied by the standards for measuring the geometrical parameters of surfaces [36, 37].

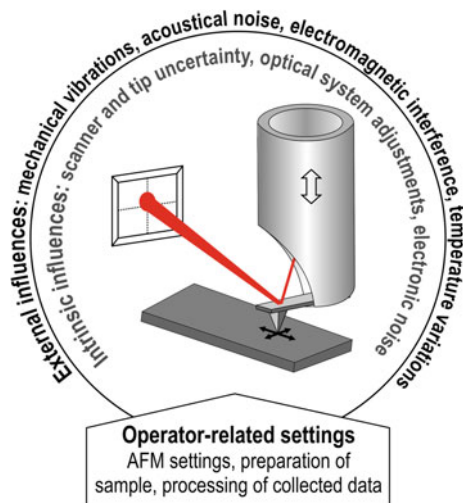
Except standardization of the very SPM, respective technical committees develop standards that regulate performing the nano-technological measurements, because transfer of technologies from the stage of researches through fabrication up to commercial market requires neatly defined estimation criteria. Metrology is called on not only control production but provide solution of matters concerning the ecological safety, legal and ethical aspects. The results of analytical researches made in Europe and USA indicate that standardization is one of key issues that bound commercial realization of micro- and nanotechnologies [38]. The respective international organizations work at these tasks. In particular, created in 2005, in the International Standard Organization (ISO), are the technical committee (TC) 229 “Nanotechnologies”, and in the International Electrotechnical Commission (IEC)—TC 113 “Nanotechnology standardization for electrical and electronic products and systems”.

At the national level, adaptation (implementation) of these standards is executed by respective authorized bodies. Leaders in development of SPM standards are Asian countries, in particular, Japan and Taiwan. In Europe, the largest activity is demonstrated by Germany, and among the countries of Former Soviet Union—Russia and Kazakhstan.

The above mentioned standards allow formulation of requirements to SPM parameters providing solution of specific tasks in diagnostics of functional materials, or, on the other hand, to determine the range of tasks that can be solved using the specific SPM method. It should be noted that technical parameters announced by a producer can be considered in this case only as an approximate qualitative indicator and must be tested [39]. Like to any measuring device, estimation of SPM should begin from construction of its metrological model. First of all, one should determine sources of uncertainties in measurements and characterize them in accordance with adopted standards. In what follows, we shall show an example of metrological estimate for the probe microscope NanoScope IIIa Dimension 3000.

There are many error and uncertainty sources in SPM, however, basic errors and uncertainties that can be observed in any SPM could be classified as follows: external influences, intrinsic influences and the operator-related ones. External factors are determined by surrounding where this facility operates. It implies stabilization of climate conditions for exploitation (temperature, humidity), protection from noise and vibrations, quality of power supply and grounding, etc. Internal factors are determined by construction features of the device and quality of their accomplishment. The operator-related ones include quality of positioning and device calibration, optimum in the choice of probes, accuracy of adjustment of

**Fig. 5** Scheme of the AFM metrological model



measurement parameters, choice of algorithms for mathematical processing the data, etc. All these uncertainties can be summarized as the structural scheme shown in Fig. 5.

It should be noted that a considerable part of external and internal sources of uncertainties is constant and can be rather efficiently minimized. For instance, usage of the systems for air cleaning and climate-control, especially in the case of SPM operating in ambient air, active or passive systems for vibro- and noise-protection, individual electrometric grounding are one of the main ways to minimize external influences.

Among the intrinsic factors, the common for SPM source of uncertainties is a scanner. Such its characteristics as sensitivity, drift and creep should be the objects of special attention. In general, metrological traceability of AFM in tasks of mapping the surface lies in piezo-scanner calibration (i.e., determination of the dependence for the displacement value on the applied voltage).

The method consists of two main parts: calibration of the scanner movement within the XY plane as well as along the Z axis. It is realized using special calibration test-structures that are made, as a rule, applying technologies of modern semiconductor electronics. Figure 6 shows an example of results obtained when calibrating the scanner of NanoScope IIIa Dimension 3000. Linearity of the scanner and accuracy of measurements were estimated using the test-structure Au/Si (received from the manufacturer of this facility) with the depth of elements  $180 \pm 3$  nm and period  $10 \mu\text{m}$ . In the image, absence of distortions in the shape of square recessions in various sections of image is indicative of the linearity in the scanner's movement, while correspondence in sizes confirms accuracy in calibration.

Analysis of these values should be carried out by using both separate profiles of cross-sections (Fig. 6b) and spectra of the spatial frequencies that can be simply

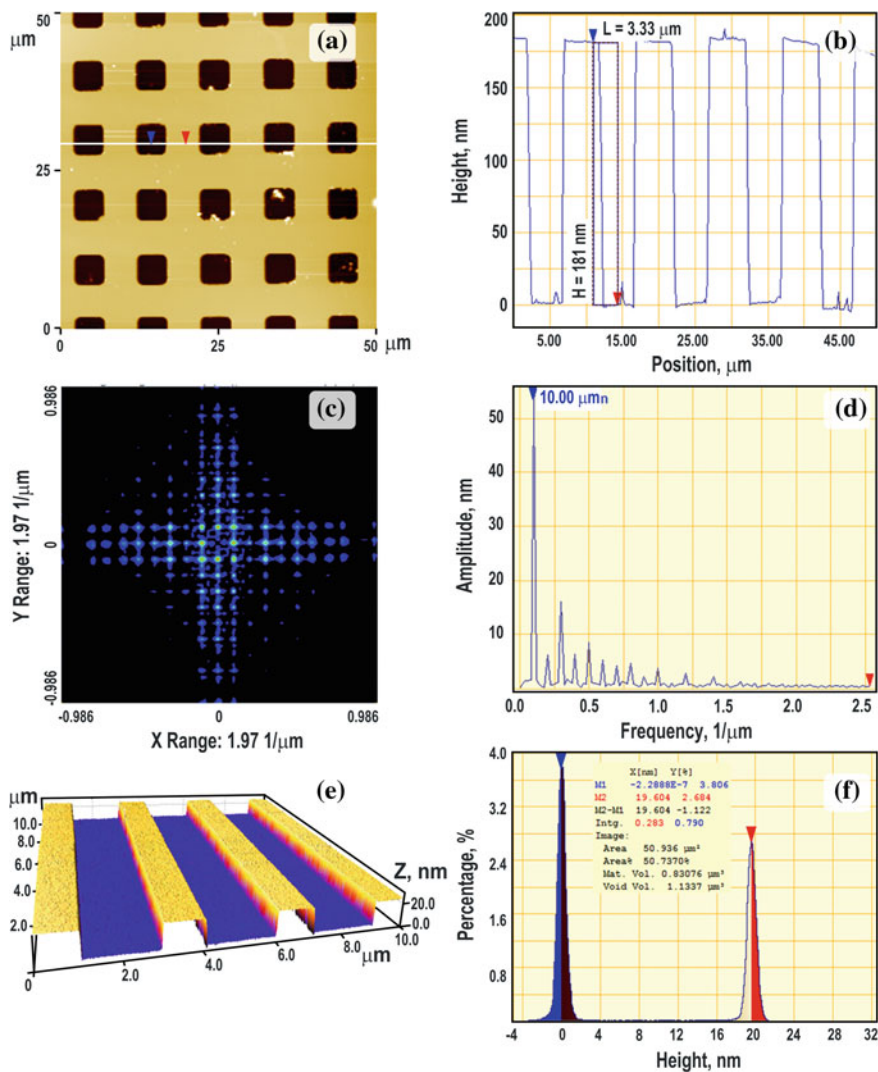


**Fig. 6** Results of AFM measurements for test structures: **a**—Au/Si. AFM map of the surface, profile of the surface along a chosen line, histogram of heights, and Fourier-transform for the height profile in this line; **b**—TGZ1 grating. 3D image for the surface map and results of the profile analysis

obtained applying the Fourier analysis (Fig. 6c, d). From the statistical viewpoint, this analysis is more reliable, as it comprises all the points of the image and not the single separated line. By analogy, vertical calibration of the scanner is based on calibration gratings TGZ made by the NT-MDT (Russia) from silicon. Shown in Fig. 6e, f are the results obtained when verifying the measurement accuracy of

vertical dimensions for surface elements by using the test grating with the height of  $19 \pm 1$  nm. Again, the analysis of results should be performed with account of local profile measurements and the histogram of heights over the whole AFM image (Fig. 6f).

### 2.2.1 The Uncertainty Related with the Piezo-Drive (Scanner)

As it follows from tests made within various dimensional ranges, boundaries of deviations for the measured values in sizes of test-structures in horizontal and vertical planes correspond to those claimed in technical performances of this SPM, which means that the accuracy of AFM measurements is no worse than the accuracy in manufacturing the test-structures. In particular, the results adduced in Fig. 6 clearly illustrate that dimensionality and orthogonality both in the XY plane and along the vertical direction in nanometer diapason of sizes are kept. The histogram of heights for the Au/Si test-object shows the most statistically probable thickness of the gold film of 181 nm (distance between two adjacent maxima). As follows from the Fourier-transform for the relief, the most typical value for the period is close to  $10.00 \mu\text{m}$ . Respectively, the height of steps in the test grating TGZ1 averaged by 20 profiles is close to 19 nm.

Being based on the performed calibration measurements, the values for boundaries of deviations in dimensions of test-structures can be adopted as respective boundaries of deviations in the nanometer range of measured sizes  $\Delta_{\text{scan}} = \pm 1$  nm. Thereof, the standard uncertainty of the scanner is equal:

$$u_{\text{scan}} = \frac{\Delta_{\text{scan}}}{\sqrt{3}} = \frac{1}{\sqrt{3}} = 0.577 \text{ nm}$$

### 2.2.2 The Uncertainty Related with an AFM Tip

A real (non-digital) spatial resolution of AFM images is determined by geometrical shape and sizes of the probe tip, as it is the probe that interacts with a sample, and the measuring system reconstructs the surface profile by using the coordinates of its tip apex. As mentioned above, in relation with that, the curvature radius of the tip apex can be commensurable with sizes of surface elements (that furthermore do not possess any axis-symmetric shape), the AFM image is a “convolution” of the tip shape and real surface relief. Depicted in Fig. 7 are 3D-AFM images of quantum wires InGaAs/GaAs recorded using the typical probe [20] with the radius of the apex close to 10 nm (Fig. 7a) and using the ultra-sharp tip [21], the radius of which is less than 1 nm (Fig. 7b). The range of vertical dimensions is 5 nm. It is seen that, due to convolution, there missed is information on a fine structure of wires. Besides, their transverse sizes are overstated. Deviations can reach 60 % of real heights. Thus, based on statistical analysis of AFM images obtained using typical and

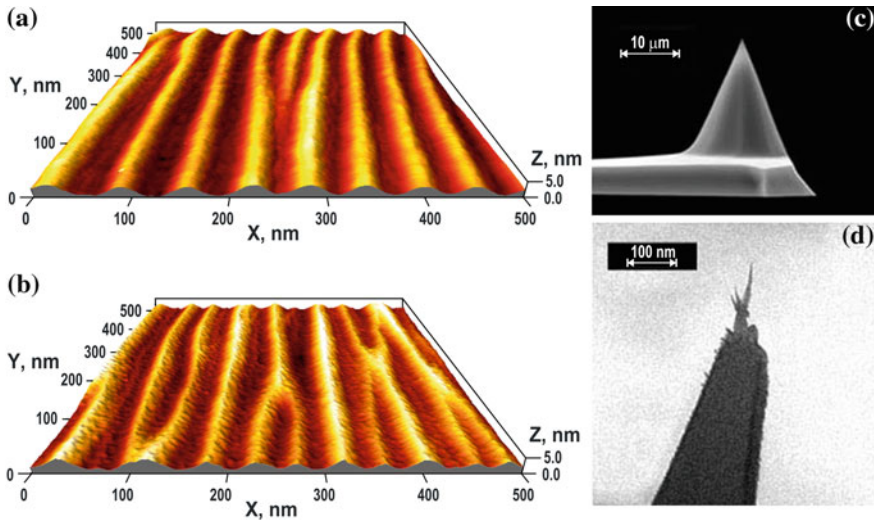


**Fig. 7** 3D-AFM image of In-GaAs/GaAs quantum wires obtained with a typical tip (a) and image of the same surface obtained with an ultra-sharp tip (b). Scanning electron microscope images of a typical (c) and an ultra-sharp tip (d)

ultra-sharp tips, the calculated value of the uncertainty for the typical probe with the apex radius of 10 nm in the sub-nanometer range (below 1 nm) is equal to

$$u_{tip} = \frac{\Delta_{tip}}{\sqrt{3}} = \frac{0.6}{\sqrt{3}} = 0.346 \text{ nm}$$

### 2.2.3 Uncertainties Related with an Optical System, Digital Electronic Parts and External Factors

When constructing the metrological model of AFM, it was noted that results of measurements can be distorted by external influences, namely: vibrations, acoustical noises, changes in the temperature of ambient medium, etc. Besides, “digital” noise and variations in the sensitivity of laser optical system can introduce some errors. The uncertainties introduced by the above factors can be estimated using the test of AFM noise amplitude on condition that effects of piezo-drive and probe are excluded. This test was realized by scanning the area with dimensions of  $1 \times 1 \text{ nm}$  (which means the practically static mode for the scanner with the maximum scanned area of  $100 \times 100 \text{ }\mu\text{m}$ ) on a freshly cleaved mica surface. The test was performed within the time range equivalent to the typical time of measurements (10 min). In these tests, it was ascertained that the noise amplitude equals to 0.05 nm.

So, it was obtained that the total uncertainty related with digital electronics, optical system of AFM, systems of vibro- and noise-protection, as well as systems of conditioning, shielding and electrometric grounding does not exceed:

$$u_{opt} = \frac{\Delta_{vibr}}{\sqrt{3}} = \frac{5 \times 10^{-2}}{\sqrt{3}} = 0.029 \text{ nm}$$

Thus, the maximum total uncertainty of measurements calculated with account of the most essential above mentioned components (which have no correlation bonds) is equal in this case to:

$$u_{total} = \sqrt{u_{scan}^2 + u_{tip}^2 + u_{opt}^2} = 0.675 \text{ nm}$$

In other conditions, the value of the measurement uncertainty will have another meaning. In this case, the ratio of sizes typical for the tip of the probe and for elements of the studied surface can be essential. For instance, in topometric investigations of nanostructural surface elements, the resolution value of the very SPM should be distinguished from that of the image. The real image resolution is determined by the relationship of scan step size and that of probe tip radius. For the apparatus accuracy of horizontal positioning in the SPM scanner higher than 0.5 nm, the image resolution (scan step) on the area  $500 \times 500$  nm, which is recorded into the data array  $512 \times 512$  points, will be close to 1 nm.

Starting from simple geometric considerations, the probe with the tip radius of 10 nm is able to distinguish two surface points with a dimple of 0.1 nm between them, if beginning from the minimum distance of 3 nm between them

$$d_{min} = (4\Delta z(2R - \Delta z))^{0.5},$$

where  $R$  is the radius of the probe tip,  $\Delta z$ —depth of the dimple. The respective resolution will reach 1.5 nm. It is clear that lowering the only scan step (for example, when recording the image of  $250 \times 250$  nm), one cannot reach a higher image resolution, which is caused by too large tip radius. At the same time, the super-sharp probe with the tip radius of 1 nm is able to provide resolution of 0.5 nm, at the scanned area of  $300 \times 300$  nm adequate to it (Fig. 8).

As seen from Fig. 8a, in the case of densely located SnTe nano-islands of small sizes (close to 5–20 nm), there takes place a considerable “tip effect” that includes both expansion of nano-islands and impossibility for the tip to penetrate into narrow dimples between them [40]. In its turn, using the ultra-sharp tip enables to eliminate both causes for distortion of data (Fig. 8b). Comparison of the measurement data obtained with the standard and ultra-sharp tips has shown that the error in determination of such important for analyses of growth processes parameter as the form-factor (ratio of the nano-islands height to the diameter of its basis) can reach 55 %, when scanning with the standard tip.

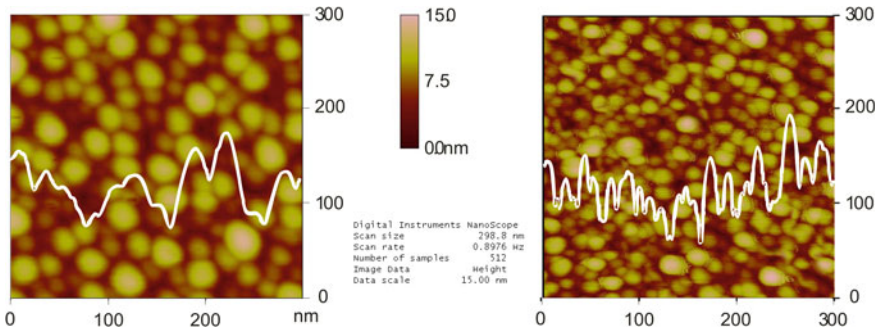
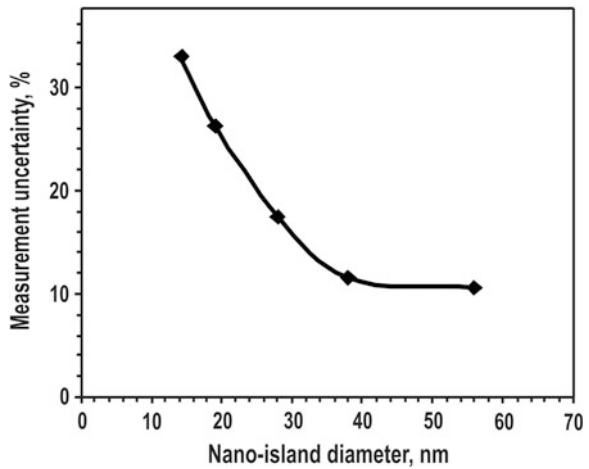


**Fig. 8** AFM image of SnTe nano-islands on BaF<sub>2</sub> obtained with standard (*left*) and ultra-sharp (*right*) tips. It is the case of dense location of nano-islands on the surface. White curves are used to illustrate transverse sections of images

**Fig. 9** Errors in measurements of diameters inherent to surface elements in dependence on their lateral sizes. Data were obtained for the silicon tip (apex radius 10 nm) using the images in Fig. 8



However, this situation is changed if investigating nano-islands with the sizes 15–60 nm, if nano-islands are located at a sufficient distances one from another (Fig. 9). The difference between images obtained using ordinary and ultra-sharp tips is related only with expansion of nano-islands (under movement, the tip penetrates up to the substrate). Analyzing the results of grain size measurements in Fig. 8, one can plot the dependence of errors in nano-islands diameters on their sizes for the case of ordinary silicon probes with the nominal tip radius 10 nm (Fig. 9).

The dependence we obtained coincides well with the approximated formula for probe effect correction [41]:

$$D = d\sqrt{(1 - 8Rh/d^2)},$$

where  $d$ ,  $h$  are the diameter and height of nano-islands derived from the AFM image.

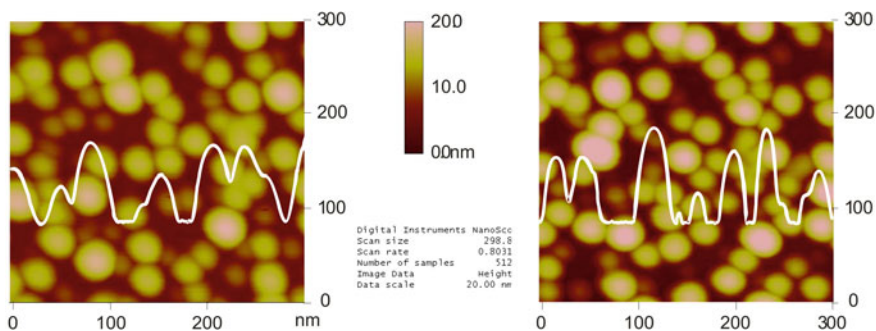


**Fig. 10** AFM image of SnTe nano-islands on BaF<sub>2</sub> obtained with standard (*left*) and ultra-sharp (*right*) tips. The case of free location of nano-islands on the surface

This equality is valid only in the case when the vertical resolution of AFM images does not depend on the probe radius, i.e., when the distance between adjacent surface elements is larger than its radius. Thus, in this case (Fig. 10) there is no necessity to use ultra-sharp tips, it is sufficient to use the standard tip for a correct analysis of surface elements.

### ***2.3 Elimination of AFM Probe Geometry on the Surface Image by Using the Method of Computer Reconstruction***

The minimization of the probe effect on SPM topometry results can be solved by two main ways. First, one can use probes with a small tip radius and a little apex angle. In this case, various technologies for sharpening ordinary silicon probes as well as technologies for additional growing up the wire-like crystals from diverse materials or carbon nanotubes at the top of probe tip are often used [42–44].

This approach provides an increase of image resolution up to the molecular level. However, in most of cases, ultra-sharp probes are efficient on surfaces with the range of heights up to 20 nm (it does not concern special probes for measurements at the vertical walls of parts with a relief of micrometer height). Besides, their high commercial cost and very limited resource prevent wide usage.

The second way is the computer software reconstruction of experimentally obtained AFM images, when tip contribution is excluded from the image, if the shape of a tip is known [45, 46]. In this approach, the key task is to ascertain the shape of the tip operation part. In this case, except a simple approach with a second order surface [45], the real shape of the tip is usually determined using special test structures [47, 48] or the so-called “blind” reconstruction based on a preliminary measured image [49–51]. The method based on the approach of the tip shape with the second order surface gives the highest error. Two other methods have their own advantages and deficiencies. For example, usage of test structures is optimal



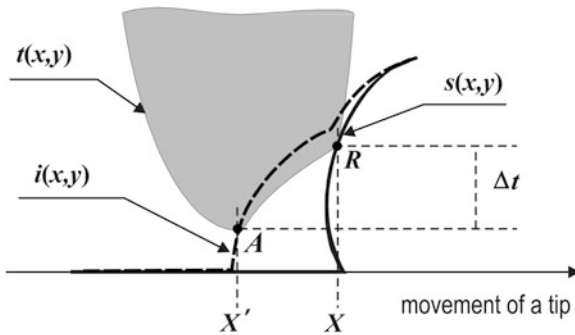


**Fig. 11** To reconstruction of a real surface by using the known shape of the tip and recorded AFM image.  $s(x, y)$  is the real surface,  $t(x, y)$ —tip surface,  $i(x, y)$ —surface in non-reconstructed AFM data. A—tip apex (the point monitored by AFM at image recording), R—point of tip-surface contact (the point determined tip-surface interaction)

when their geometrical parameters are not only less than the probe tip ones but are commensurable with components of the relief that should be studied. Besides, this way for testing the tip shape requires additional test measurements before and after topometric surface investigations and is inefficient if the tip shape is changed in the course of measurements. In its turn, the tip shape reconstructed using the blind method has a maximum possible size that still provides obtaining the image under reconstruction [49]. The scheme of method is shown in Fig. 11. Main idea is to find minimal tip-surface distance within the region under the tip ( $X'X$ ) and correct the height value in this point by  $\Delta t$ .

Thus, the known ways to minimize the probe effect are not self-sufficient, and correct results of topometric investigations of nanostructured surfaces is possible only being based on clear understanding their advantages, deficiencies and limits of usability.

Among the mentioned above methods for obtaining the tip shape, blind reconstruction is the most efficient one. This method does not require any additional measurements, there is no necessity in export/import of data that set the tip surface shape, reconstructed part is the most essential imaging tip part, etc. However, with all its advantages, this method has definite limitations that can essentially influence the results of reconstruction. For instance, if the surface has a regular shape (diffraction gratings, etched monocrystalline surfaces, quantum dots of close sizes and shape, and so on), then the set of possible limits for tip sizes is limited, which can result in imaging the regular relief elements in the shape of sharp peaks; when analyzing smooth surfaces (dispersion of heights  $Z$  for which is close to 2–3 nm), the set of possible limits for tip sizes comprises only a very small range [40]. It leads to an unlikely value of the tip radius; apparatus effects of various kinds, which are not related with the probe but take their place in the image (local spikes, noises, scanner drift, too large or too small force of probe-surface interaction, etc.) and can contribute to the tip shape reconstructed by the software.

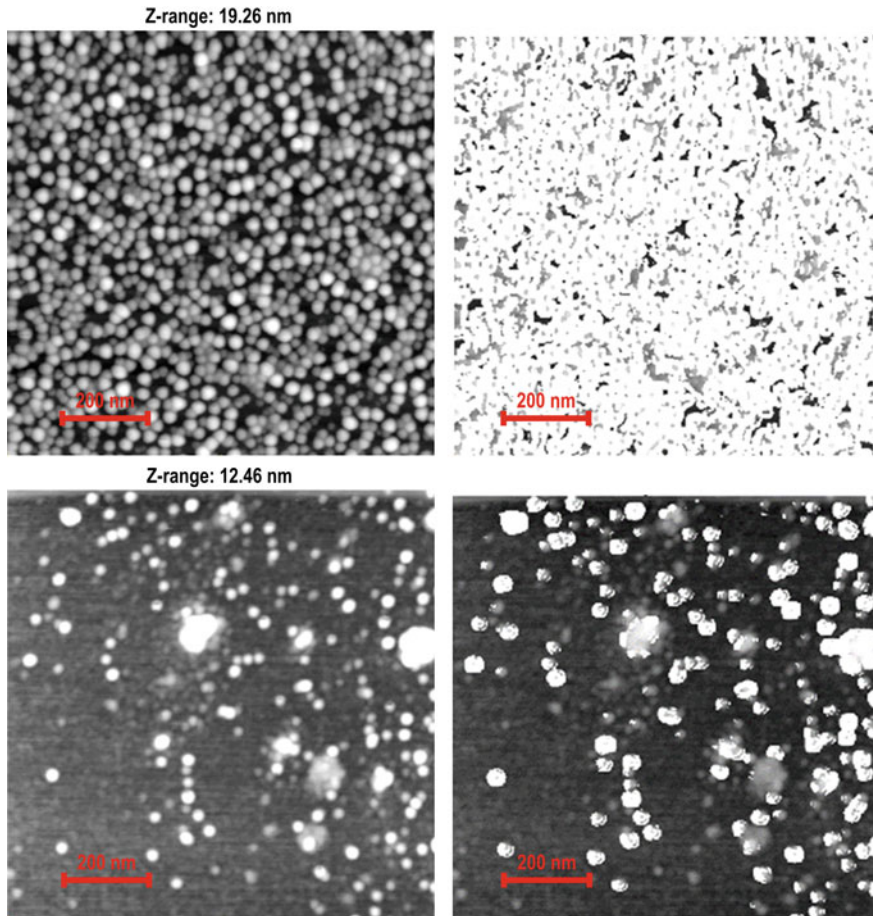


**Fig. 12** Non-reconstructed AFM images (*left*) and their uncertainty maps (*right*) for surfaces with different location and shape of nano-islands

It should be also noted that the reconstructed image, independently of the way used to obtain the tip shape, can exactly coincide with the real sample surface under condition that in the scanning process the tip touches only one point of the surface in each time moment. As a consequence, the tip can touch every point of the surface in this process. In other case, there remain the so-called “blind areas” on the surface, and their correct reconstruction is impossible. Their shape and sizes depend on the tip geometrical shape. In particular, for the ordinary silicon tip with the quadrangular pyramid shape, these blind areas are those located with the angle less than the angle at the pyramid apex  $11^\circ$  with respect to the vertical, or pores that are narrower than the tip. The algorithm for reconstruction of AFM images allows to easily depict these surface blind areas as uncertainty maps (Fig. 12),

which can serve as a criterion of usability for the tip with given geometry. If the area of blind zones (marked with white color) reaches more than 60 % of the total image area, then the reconstruction program is incorrect, and more sharp probes should be used.

The example of usability of the software image reconstruction for a surface with the area of blind zones close to the acceptable limit in the sample of SnTe with nano-islands is shown in Fig. 13. In this case, the zone at the basis of nano-islands is blind, therefore, reconstruction does not lead to changes in the sizes of the nano-island basis. In relation with it, when analyzing nano-island sizes as lateral characteristics, it is more correct to use the diameter of the nano-island section at the half of its height (see insets in Figs. 13a and b), because at this level reconstruction approaches to the sizes and shape of the real ones, and, if necessary, the basis size can be calculated using extrapolation of the nano-islands shape.

For comparison, shown in Fig. 13c is the image of the same sample obtained in the scanning electron microscope Zeiss Ultra 55 with the resolution close to 1 nm. It is seen that contrary to the non-reconstructed image (where nano-islands have the shape of hemispheres), nano-islands in the reconstructed one are depicted more correctly—as triangular pyramids (for a good layout, see the fragment of 3D representation), which fully coincides with the electron-microscopic data. Some comparison of scanning electron microscope and AFM imaging could be found in [52].

### 3 AFM Investigations of Semiconductor Quantum Dots Shape and Surface Ordering

Topometrical AFM investigations provide an important information concerning peculiarities of growth processes at nanostructures fabrication. For example, we investigated self-assembled nano-islands in heteroepitaxial GeSi systems grown by molecular beam epitaxy [53]. Strain-induced self-assembled nano-islands in heteroepitaxial GeSi systems have attracted much attention because they offer the possibility of realization of new optoelectronic devices based on the well-developed Si technology. The large lattice mismatch between Ge and Si (4 %) results in the growth of ultrathin Ge layers on Si substrates being driven by the Stranski–Krastanov mechanism. However, this mechanism gets complicated under Ge–Si composition transformation at certain growth conditions.

We have used AFM and micro-Raman scattering to study how the density, volume, shape and composition of Ge islands change depending on the thickness of the deposited Ge layer and the Si substrate temperature. The assertion that bimodal island size distribution is related with two (pyramid-like and dome-like) possible shapes of their equilibrium configuration is confirmed. The island composition is shown to be of mixed  $\text{Ge}_x\text{Si}_{1-x}$ -like type due to surface diffusion of Si atoms from the substrate. This process is strongly enhanced when temperature

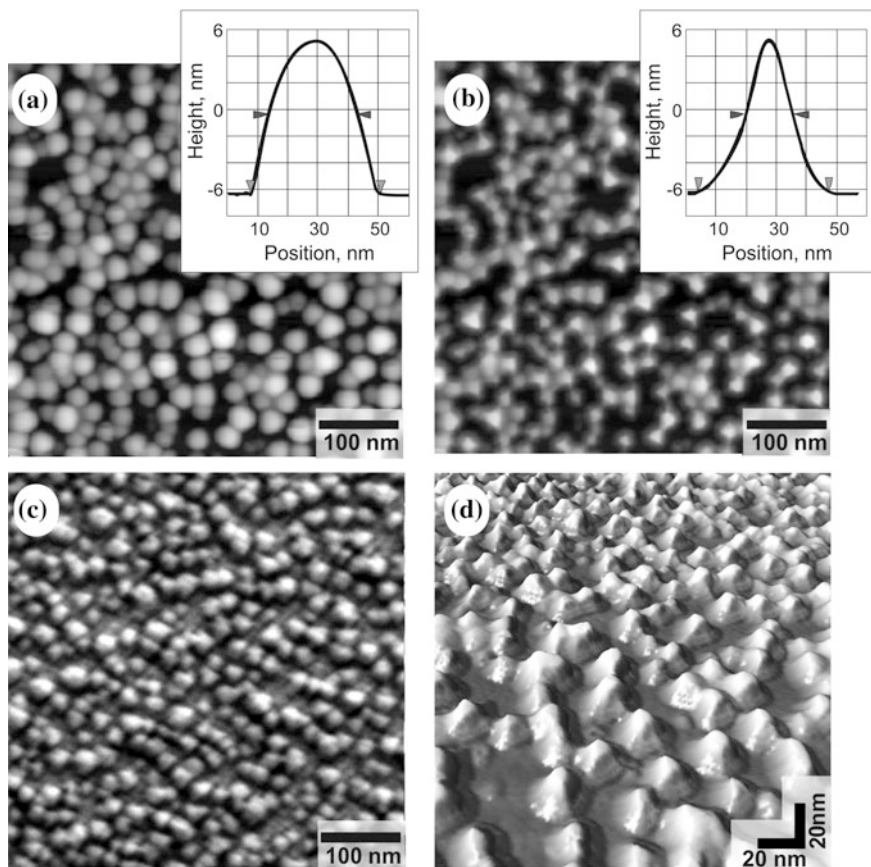


**Fig. 13** AFM images of the surface fragment and nano-islands section for the system SnTe/BaF<sub>2</sub> before (a) and after (b, c) computer reconstruction; (d)—image of the surface obtained in the scanning electron microscope with high resolution ( $\sim 1$  nm)

increases. As a result, the stability range of the pyramid-shape island volumes at the measured deposition rate becomes substantially wider. Thus, it is only at low temperature that one can obtain a high concentration of Ge islands on Si(100) surfaces with a narrow size distribution.

The nature of the bimodal size distribution can be explained in two ways. In the first model, one considers that a specific minimum energy configuration corresponds to each particular shape of strained islands, and an activated transition can occur between the two configurations [54]. The key idea of the second model is that the chemical potential of an island undergoes an abrupt change as the equilibrium shape changes from pyramid-like to dome-like [55]. This occurs at a well-defined volume, the one at which the energy of the dome becomes lower than the energy of

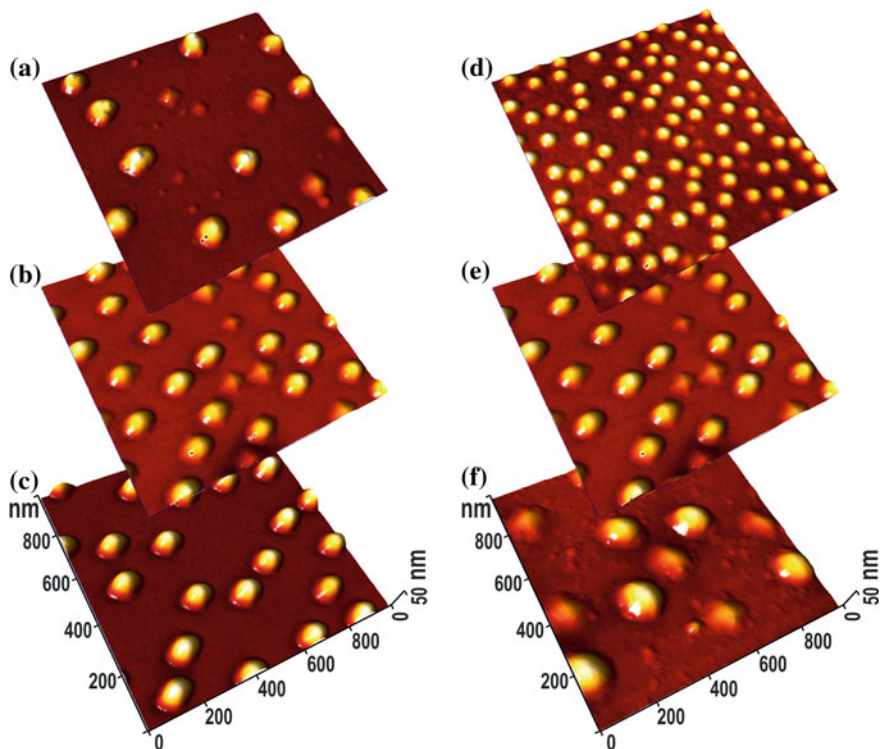


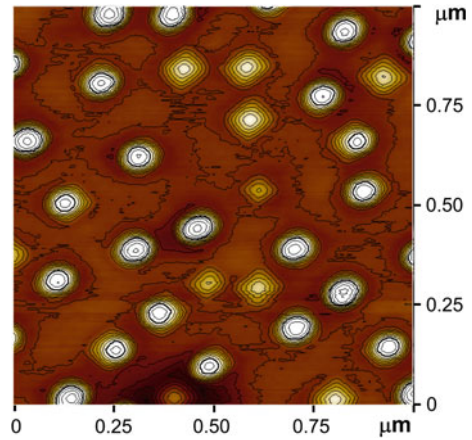
**Fig. 14** 3DAFM images of self-organized nano-islands grown at 700 °C with the nominal thickness of Ge wetting layers 5.5 ML (a), 9 ML (b) and 11 ML (c). The set of AFM images of nano-islands grown at different temperatures (600, 700 and 750 °C, correspondingly d, f and g) from 9 ML Ge wetting layer

the corresponding pyramid. In any case, the experimental data concerning the distribution of both the shape and size of the islands are of great importance.

AFM images taken for Ge layers of three different thicknesses are presented in Fig. 14a–c. The growth temperature was 700 °C and the growth rate was 0.015 nm/s. Another set of AFM data taken from a series of Ge layers with the nominal thickness of 9 ML, but grown at different substrate temperatures is shown in Fig. 14d–f. The presence of pyramid-like and dome-like islands is clearly shown in Fig. 15 for the 9 ML sample grown at 700 °C.

Plotted in Fig. 16 are the volume distributions of islands presented in Fig. 13. A comparison of Figs. 16a–f demonstrates an important qualitative difference between the island shape transformations occurring in these two series of samples. When the Ge layer thickness increases from 5.5 up to 9 ML (Fig. 16a–c), the critical volume at which the pyramid–dome transformation happens does not change. This volume is about  $4 \times 10^4 \text{ nm}^3$ , and is shown by an arrow in the figure.

**Fig. 15** 2D AFM image of the 9 ML sample grown at 700 °C. Relief is shown by isolines with 2 nm height steps



One may also consider this critical volume to remain constant even for  $d_{\text{Ge}} = 11$  ML, when all pyramids disappear. In this case, all the islands become dome-shaped and have a big average volume (about  $12 \times 10^4 \text{ nm}^3$ ).

When the deposition temperature is increased, the situation becomes quite different Fig. 16d–e). The critical volume of the pyramid–dome transformation shifts strongly toward bigger volumes, and at 750 °C the pyramid-shaped islands are predominant. We believe that this change in the island shape distribution is due to surface diffusion of Si atoms from the substrate to the bottom of the islands [56]. As a result, the islands take on a mixed  $\text{Ge}_x\text{Si}_{1-x}$  composition. The presence of shallow grooves near the bases of the dome-shaped islands that can be seen in the AFM images may serve as support of the mechanism for alloy formation in the islands.

Using Raman Scattering, we have studied the relationship between the island Ge–Si composition and their strains. The results averaged over each sample including islands of different shapes are presented in Table 1. The island compositions for samples with different thicknesses grown at the same temperature are very close. At the same time, as the temperature is increased, the silicon content in the islands grows considerably due to easier diffusion of Si atoms. Since the high stress near the bases of the islands favors intense Si diffusion, this mechanism is very important when the incipient pyramids develop.

To control the strain value in the Si–Ge heterosystem, the  $\text{Si}_{1-x}\text{Ge}_x$  buffer sublayer is used [57–60]. In this case, the areal density of the islands increases with increasing Ge content in the  $\text{Si}_{1-x}\text{Ge}_x$  buffer layer. As the areal density of the nano-islands increases, the spacing between the islands becomes comparable to their size, and lateral interaction between the elastic strain fields of neighboring islands can occur. This interaction promotes in-plane ordering of the islands. On the other hand, the presence of spatially nonuniform elastic strain fields leads to the enhanced importance of interdiffusion processes causing an anomalously

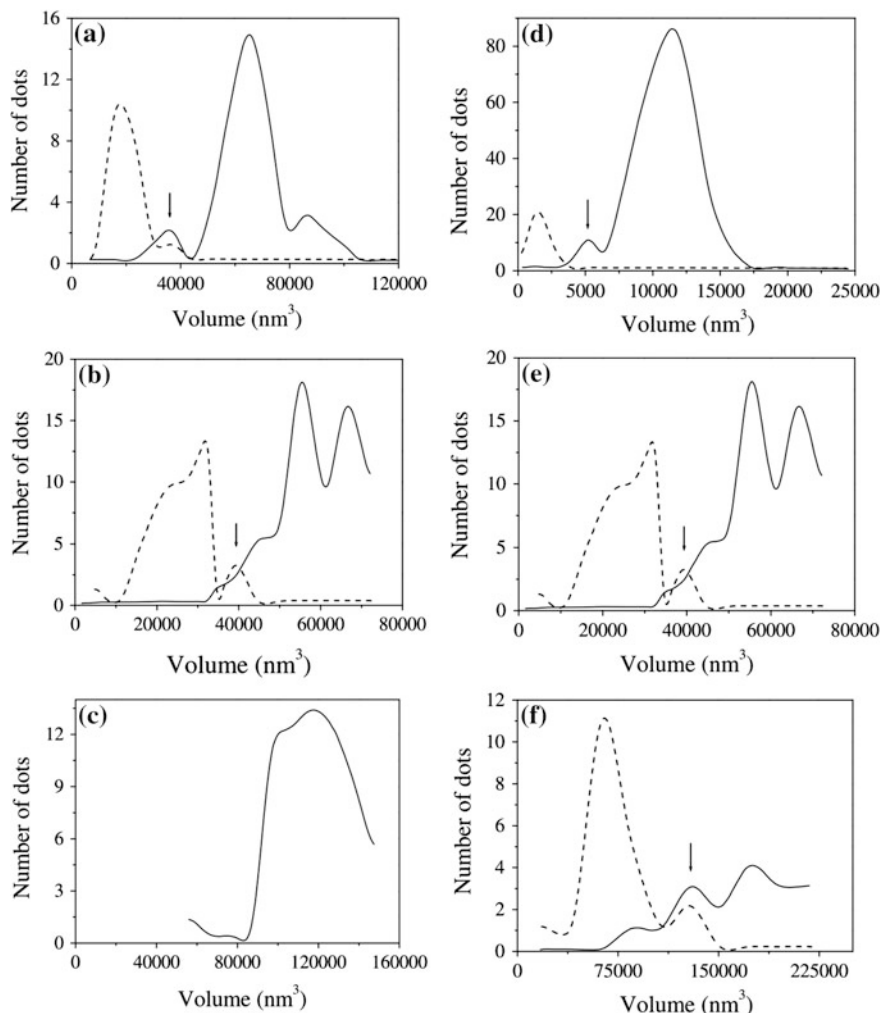


**Fig. 16** The dependence of pyramid-shaped (*dashed curve*) and dome-shaped (*solid curve*) island number on volume for samples grown at 700 °C using various thickness of Ge wetting layer (**a** 5.5 ML; **b** 9 ML; **c** 11 ML) and grown from the 9 ML Ge wetting layer at 600, 700 and 750 °C (**d–f**, correspondingly)

intense atomic flux from the buffer sublayer to the islands, in which partial relaxation of elastic strains takes place.

AFM data presented in Fig. 17 illustrate the lateral self-ordering in single layers of SiGe nano-islands grown on strained Si<sub>1-x</sub>Ge<sub>x</sub> buffer layers of different thicknesses. Surface images and corresponding statistical analysis for the control spots corresponding to 9–11 MLs of Ge deposited during the process of island formation are shown.

**Table 1** Composition ( $x$ ) and strain ( $\varepsilon$ ) of the  $\text{Ge}_x\text{Si}_{1-x}$  islands investigated, as it follows from RS measurements

ML	T (°C)	$x$ , Ge content (%)	$\varepsilon$ , strain (%)
9	600	$0.73 \pm 0.04$	$-1.3 \pm 0.3$
9	700	$0.63 \pm 0.01$	$-0.8 \pm 0.1$
9	750	$0.43 \pm 0.02$	$-1.0 \pm 0.2$
5.5	700	$0.57 \pm 0.01$	$-1.0 \pm 0.1$
11	700	$0.56 \pm 0.02$	$-1.2 \pm 0.2$

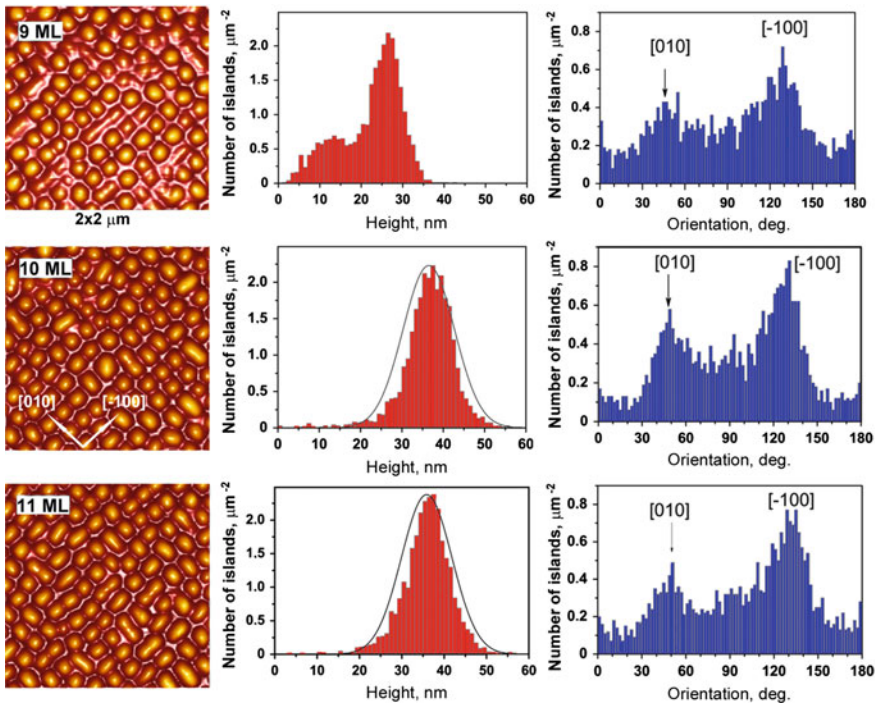


**Fig. 17** AFM images of the surface of the structure and histograms for the island heights and the major axis orientation of the island base ellipse for 9–11 MLs of deposited Ge

For 9 MLs of Ge, we find a bimodal distribution of the sizes and shapes of the islands, which are of the hut-cluster and pyramid types. An increase in the nominal thickness of deposited Ge causes transition to a unimodal distribution of dome-shaped islands for 10 MLs of Ge and a further narrowing of this distribution for 11 MLs of Ge. To some extent, the anisotropy in the shape of the island base is indicative of the intensity of elastic interaction between the islands and of the diffusive mass transfer. Thus, for 11 MLs of deposited Ge, the peaks in the distribution of island orientations (i.e., orientations of the major axes of the ellipses



approximating the shape of the island bases) are more pronounced (Fig. 17). This is an evidence for a higher degree of anisotropy of the diffusion processes taking place in the process of island formation. It is also important to note that the two maxima in the island orientation distributions are separated by  $\sim 82^\circ$ ; i.e., the lateral orientation of the islands deviates somewhat from the  $[-100]$  and  $[010]$  crystallographic directions.

The number and arrangement of peaks in two-dimensional (2D) autocorrelation functions (Fig. 18) built over the  $10 \times 10 \mu\text{m}$  scans give clear evidence of the formation of a characteristic two-dimensional grid in the arrangement of nanoislands. The islands are oriented along directions close to  $[010]$  and  $[-100]$ . The occurrence of three peaks in the profiles taken along the two directions shown in Fig. 18b is indicative of the short-range order in the mutual arrangement of the islands up to the third nearest neighbor. It is most pronounced for 10 MLs of deposited Ge. In this case, a fourth order 2D autocorrelation peak is observed, which gives the evidence of a better defined periodicity in the island arrangement. The spacing between the peaks in the autocorrelation function profiles corresponds to the average distance between the islands in a given direction.

The role of diffusion during the process of island formation could be estimated using analysis of island volumes with increasing thicknesses of deposited Ge. The amount of material in the islands exceeds the nominally deposited amount of Ge by factors of 3.3 and 5 corresponding to 9 and 11 MLs, respectively. It means that up to 60 % of the strained SiGe buffer sublayer is transferred to the islands. Note that in the case of conventional high temperature ( $\geq 500^\circ\text{C}$ ) epitaxy on top of the Si buffer, this difference, caused by the diffusion of Si from the buffer layer, can be as large as tens of percent only. Such a huge flux of diffusing atoms at a temperature considerably lower than the material's melting point can only be explained with account of the stimulating role of a nonuniform elastic strain field (the Gorsky effect [61]), the gradient of which in the studied structures with nanoislands may be very high. This strong diffusion of material into the islands during the process of their formation leads to considerable changes in the nominal composition of the layers and strains in the system. It is also evident that kinetics of the diffusion process considerably affects the resulting structural morphology.

Strain-driven self-assembly has matured into a promising method for fabrication of quantum dot nanostructures for semiconductors of various types. Epitaxy of III-V system has attracted more attention due to the unique physical properties of QDs as a zero-dimensional quantum confined system and the variety of applications in electronic and optoelectronic devices (tunable, high-efficient QD lasers [62, 63], single or multicolored QD photodetectors [64–66], etc.).

However, more complex multi-component systems as well as strongly anisotropic structures are not completely described by the simplified basic model of Stranski-Krastanov growth mode. Elastic properties of the bulk crystal lattice and surface mass transport have a significant impact on the QD growth [67, 68].

So, in the case of multi-layer structures of InGaAs QDs, additional effects must be considered namely: the strain distribution through the spacer layers, In migration on the surface during the capping process, and possibly surface roughening

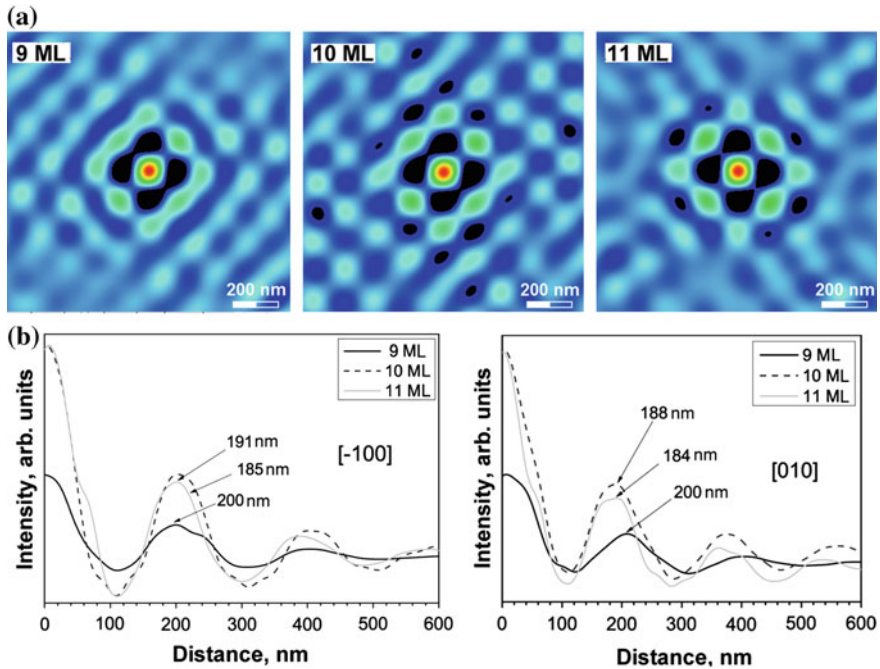


**Fig. 18** **a** Autocorrelation maps obtained from AFM scans of the structures under study for 9–11 MLs of deposited Ge **b**. Profiles of the autocorrelation maps along the directions [010] and [-100]

throughout the deposition of the spacer layer. The AFM surface diagnostic of these structures plays a very important role for optimization of technological processes and fundamental investigations in physics of low-dimensional structures.

The good starting point for surface anisotropy estimation by AFM could be micro-size defects, known as oval defects typical for MBE grown III-V structures [69]. We investigated surface morphology of micro-size defects on the surface of various high-index GaAs substrates [70]. The investigated surfaces were the top layer of 1- and 17-period  $\text{In}_{0.45}\text{GaAs}_{0.55}/\text{GaAs}$  structures with quantum dots. These structures were characterized by formation of oval defects on (100) surfaces, and micro-size defects possessing the shape of multifaceted pits and hillocks on  $(n11)A/B$  ( $n = 7, 5, 4, 3$ ) surfaces. We have illustrated that their distribution and density do not depend on the substrate orientation, while the shape and orientation of the micro-size defects depend on the crystallographic orientation of the substrate. This dependence was determined to be the result of anisotropy of surface diffusion and surface elastic properties. Anisotropy of elastic properties of high-index surfaces was found to be the dominating factor in determining the shape of micro-size defects.

Oval defects (ODs) are the main type of morphological defects found on GaAs films grown using the MBE method on GaAs substrates with (100) orientation.

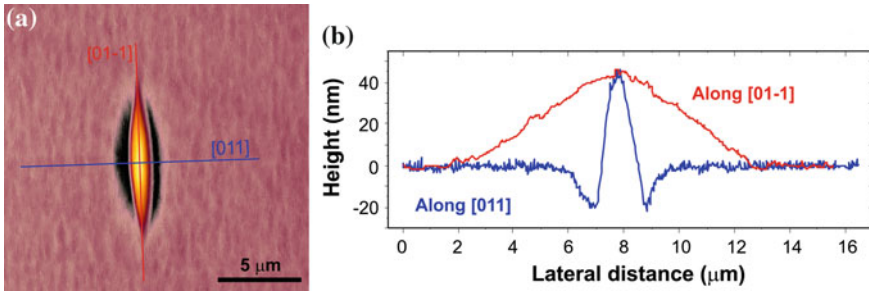


**Fig. 19** AFM image emphasizing one oval defect (a); corresponding height profiles of the oval defect (b)

When using a substrate with (100) orientation, the long axis of the OD lies along the  $\langle 011 \rangle$  direction [69] (Fig. 19). Typical dimensions of these defects are of the order of several micrometers depending on the epitaxial layer thickness and their density can reach  $10^4 \text{ cm}^{-2}$ , in our case.

On the  $(n11)$ A/B surfaces, micro-size defects form as dimples having a multifaceted shape, and in all cases, possess the (100) facet (Fig. 20). As we change the growth surface from (311) to (711), the observed micro-size defects are basically similar to those observed on the (311) surface. However, the tail at the defect base is reduced in length, while the angle at the apex, formed by the defect facets, is increased. Crystallographic orientations of micro-size defects were determined using X-ray diffraction in symmetric and asymmetric reflections. It confirms the constant orientation of defects tails.

As seen from Fig. 21, the crystallographic orientation of micro-size defects coincides with the direction of the largest elastic constants. In multilayer structures grown on GaAs(1 0 0) substrates, the micro-size defects are oriented in the direction  $[01-1]$ , which coincides with the direction of the largest In/Ga adatom diffusion [71, 72]. When changing the surface orientation from (100) to (711), the anisotropy of the surface elasticity modulus is considerably reduced. In our opinion, it is the effect, which is responsible for the change in the micro-size defect shape. That is, for the (711)B surface, the relative magnitude of anisotropy of the elasticity modulus is smaller than that for (100) and (311), which results in round shape defects (Fig. 21c). On the other hand, a decrease in the defect tail length with increasing  $n$ -index on GaAs  $(n11)$  substrates can be explained stemming from purely geometrical grounds. The defect front facet coincides with the (100) crystallographic plane that has been neither smoothed nor overgrown in the course of the structure growth. It is most probable that the opposite defect facet is also limited by a crystal plane, but it is strongly subjected to diffusion smoothing and partial overgrowing. However, the angle between the front and back facets of multifaceted defects on  $(n11)$  surfaces remains approximately the same. As a consequence, when the  $n$ -index reaches high values, the  $(n11)$  surface will cut a

larger and larger part of the defect tail, and, as a result, the defect shape will be more rounded, which is what observed experimentally.

We observed a clear tendency in multilayer structures to form laterally ordered arrays of QDs (Fig. 21). Depending on the substrate surface orientation, one can obtain QDs ordered along the  $[01\bar{1}]$  direction (QD chains) (Fig. 21a) [73] or laterally ordered networks of nearly equal-distant QDs [74] (Figs. 21b, c). Here, the defect orientation and symmetry have a one-to-one correlation with the position of QDs on the surface. The cell dimension of the QD lateral network on the less anisotropic surface (711)B is less than that on the (311)B surface, and the shape of the lateral cell is close to the rhombus one. Lateral self-ordering of the QDs in multilayer structures is most probably caused by formation of periodically changing field of elastic strains as well as an accompanying redistribution of the impurity-defect composition of the growth surface. The influence of an elastic strain far-acting field on QD lateral ordering is indirectly confirmed by Fig. 21b where the defect strain field causes fluctuations in QD lateral ordering. In the defect core region (i.e., in the ranges of the largest strain and compositional gradients), several QD rows exactly follows along the defect facet orientation directions, that is the lateral QD arrangement “feels” the shape of the strain field distribution around the defect.

The strain fields developed in the growth direction of multilayer  $\text{In}_{0.45}\text{Ga}_{0.55}\text{As}/\text{GaAs}$  structures determine the size and lateral arrangement of (In,Ga)As QDs, and their value considerably exceeds the strain fields and concentration fluctuations formed around micro-size defects. The latter is developed during QD growth on the micro-size defect surface and confirmed by the appearance of small fluctuations of their lateral arrangement (QD chains and networks cover defects without significant transformations). The studied micro-size defects can be used to determine surface crystallographic orientation, as indicators of anisotropy inherent to surface physical (elastic) properties. Meanwhile, sets of microspheres with various orientations can be used as a playing field to explore QD growth processes.

Further, we have investigated in details a lateral ordering scenario of QDs as a function of substrate orientation and the number of vertical periods. Because of the statistical nature of Stranski-Krastanov growth mode, self-assembled dots are sometimes not very uniform in size, shape, and interdot spacing. This fact poses significant limitations for device applications. While self-assembled QD multilayers have shown that the vertical alignment throughout subsequent layers can be engineered to be nearly perfect, the lateral ordering tendency was found to be much less pronounced. A different type of arrangement, i.e., an anticorrelation of dots on subsequent layers, has been observed for II–VI, IV–VI, and III–V systems [75, 76].

It was further demonstrated that the elastic anisotropy of the materials plays a crucial role for the lateral and vertical self-organizations in QD superlattices [77]. It includes both anisotropy effects of the strain fields and adatom diffusion, as well as the elastic interaction of neighboring QDs. Generally, the balance between strong repulsive elastic interaction of adjacent initial dots and, on the other hand, the minimization of the total strain energy acts as the main driving force for the

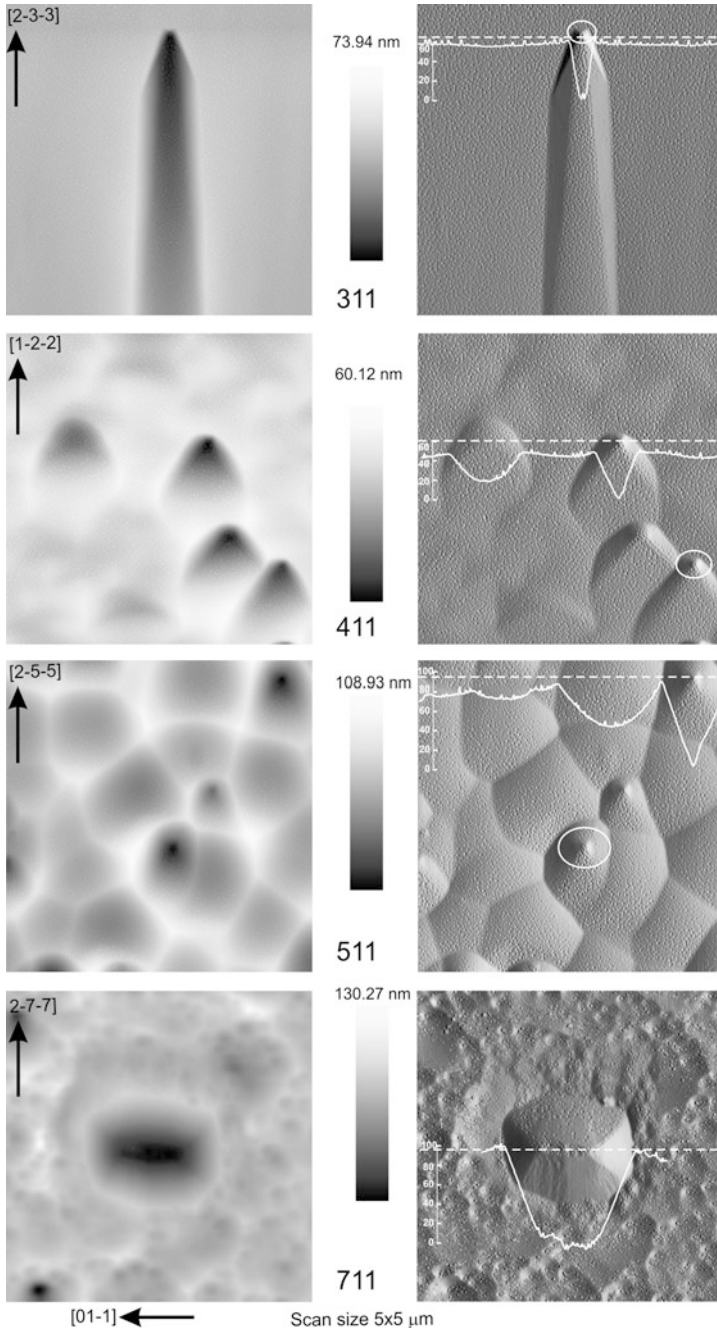


**Fig. 20** Surface height maps (*on the left*) and derivatives ( $dz/dx$ ) of AFM images (*on the right*) of typical microsize defects on the surface of  $\text{In}_{0.45}\text{Ga}_{0.55}\text{As}$  (7 ML) layer on GaAs ( $n11$ )B substrate. There pointed are the sections (profiles) of surfaces along the dotted lines. Empty ovals point the defect cores. Quantum dots can be seen on the surfaces and on the defects

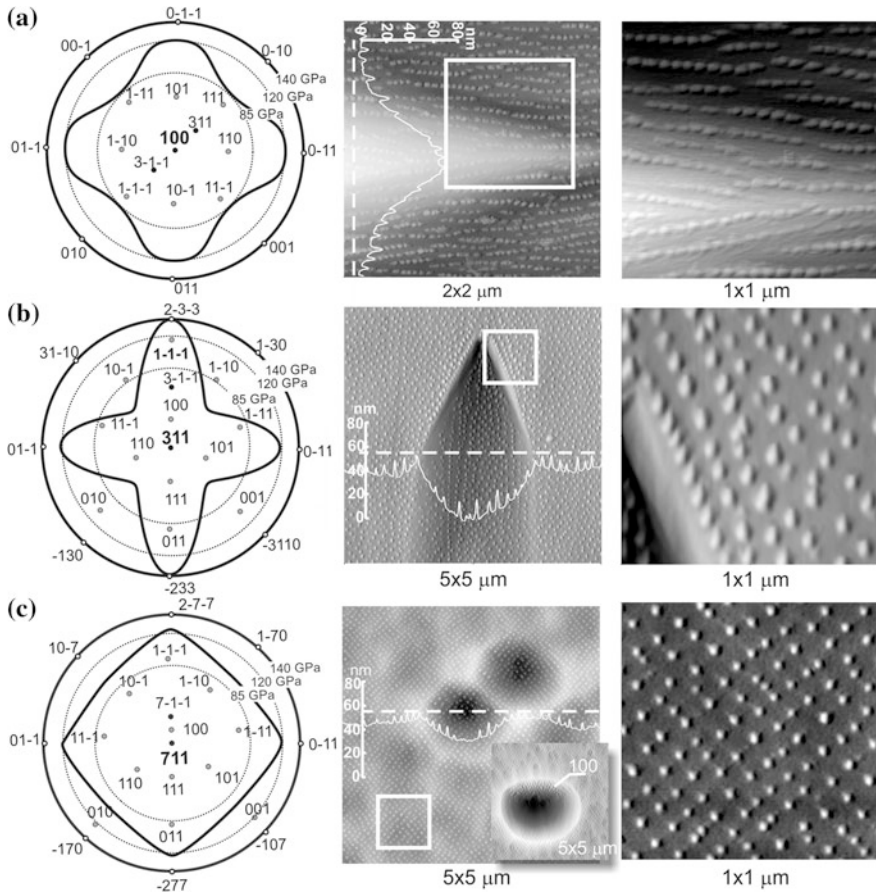


**Fig. 21** Schematic representation of stereographic projections with indication of the elasticity modulus value distribution along crystallographic directions (*left*) and micro-size defect AFM images with cross-sections along dotted lines for the surface of 17-period  $\text{In}_{0.45}\text{Ga}_{0.55}\text{As}/\text{GaAs}$  structure when the substrate orientation is: **a** (100), **b** (311)B and **c** (711)B. Images of an enhanced resolution that illustrate formation of QD patterns are shown at the *right*

lateral and vertical self-assembling. Investigating the strong impact of high index surfaces on formation of ordered QD arrays is expected to provide more detailed understanding of the underlying growth kinetics. Thus, it might help to improve physical properties of low-dimensional structures.

Our AFM studies indicate no well-ordered QD arrangement at the surfaces of the 1.5 period structures [78]. At the same time, the differences in density, shape, and size of QDs grown on differently oriented substrates were well pronounced. A variation of the growth surface from (100) to (911)B, (711)B, (511)B, and (311)B (increase of the angle of surface ( $n11$ ) deviation from the surface (100)

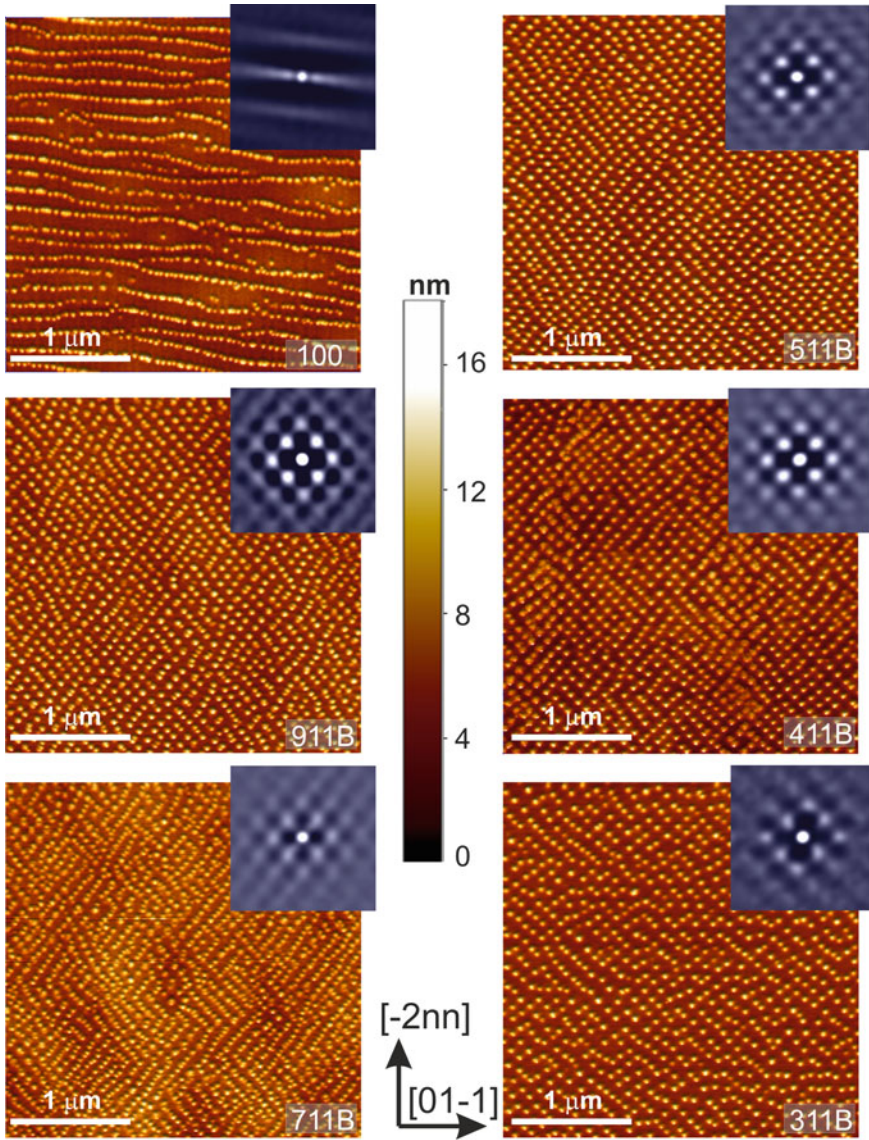


**Fig. 22** AFM images of  $\text{In}_{0.4}\text{Ga}_{0.6}\text{As}/\text{GaAs}$  QDs 16.5 periods grown on GaAs substrates of the following orientations: (100) (a), (911)B (b), (711)B (c), (511)B (d), (411)B (e), and (311)B (f). The 2D autocorrelation functions are shown in insets

toward (111)) yields the general trend to increase the QD size, while the QD density decreases.

While increasing the number of periods up to 16.5, the degree of the QD arrangement considerably improves for all probed substrate orientations. Figure 22

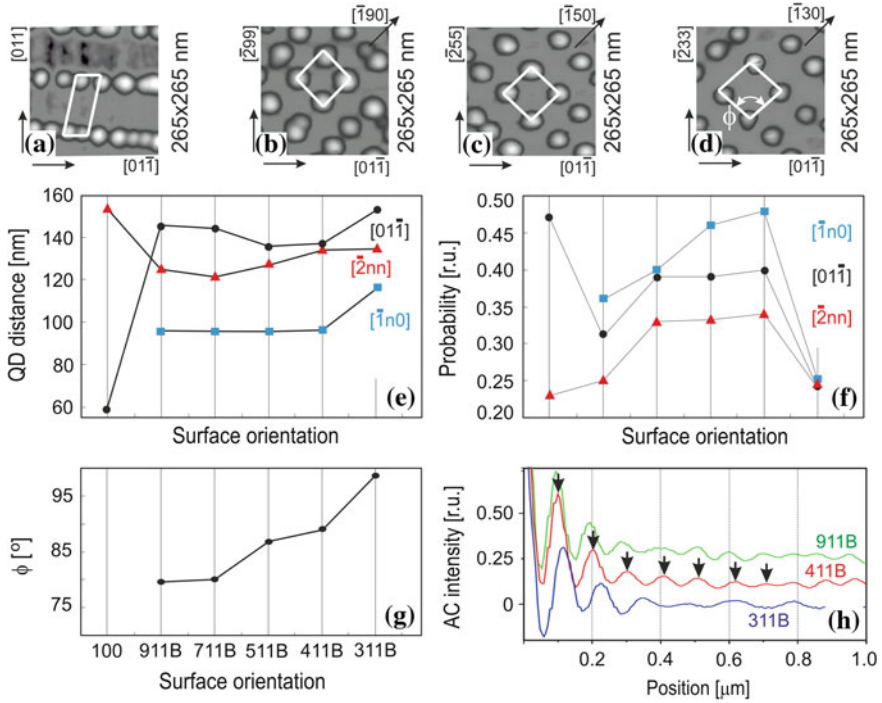


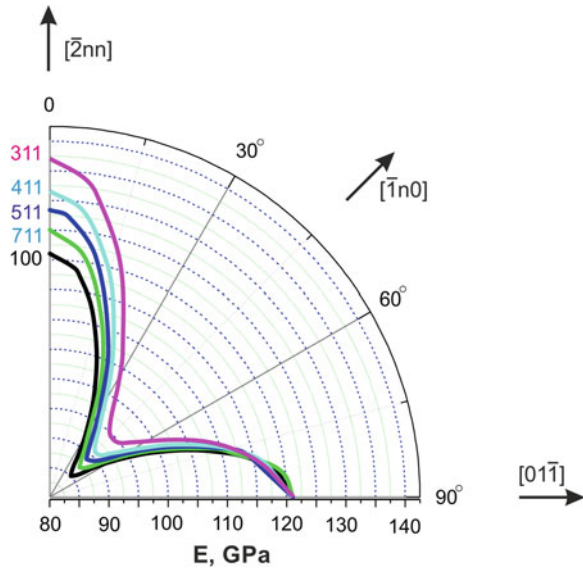
**Fig. 23** **a–d** depict surface unit cells on GaAs(100) and (n11)B, where  $n = 9, 5, 3$ ; **e–g** plots as a function of the surface orientation the dot-dot distance, probability of QD nearest neighbor occupation along the directions of preferred ordering, and characteristic angle  $\phi$ ; **h** plots the autocorrelation functions of the QDs curves are offset for a better view

depicts corresponding AFM images of QDs on high index surfaces, as well as their autocorrelation analysis insets. The presence of peaks up to the fourth order in 2D autocorrelation analysis proves highly correlated QD ensembles. Further, on the autocorrelation analysis indicate a lateral QD arrangement along two preferred directions at the surface. In order to quantify this effect, we have defined a surface unit cell (Fig. 23) by taking into account a coordination shell with the three nearest neighbors of QD.

However, the most obvious feature of the QD multilayers seems a systematic impact of the substrate orientation onto the QD lateral ordering. Figure 23e presents mean QD-QD distances at the top surface along  $[01\bar{1}]$ ,  $[\bar{2}n\bar{n}]$ , and  $[\bar{1}n0]$ , whereas these most preferred directions and the QD-QD distances have been extracted from the autocorrelation analysis. Interestingly, we found that the characteristic directions of the QD ordering at the surface correspond to the form of fourfold symmetrical anisotropic distribution of Young’s modulus (Fig. 24), calculated by us for each of the surfaces according to [79].



**Fig. 24** Angular distribution of the elasticity modulus for different GaAs( $n11$ ) substrate orientations ( $n = 7, 5, 4, 3$ ) and GaAs(100)



The probability of this kind of QD positioning determined from autocorrelation data is shown in Fig. 23f. It can be clearly seen that the 2D QD lattice of a good quality should be formed on (411) and (511) high index surfaces. The elastically softer  $[-1n0]$  direction demonstrates the best QD ordering for all investigated substrates and accordingly stiffer directions have a lower probability of QD ordering. It seems that surface elastic anisotropy dominates the QD lateral ordering, whereas QD's elastic interaction in dense arrays and QD shape and size play a second role.

From the comparison of Fig. 23g, which shows the opening angle  $\phi$  of the defined unit cell, and Fig. 24, one can see that the QD-QD distance along the elastically stiffer  $[-2nn]$  direction (the largest Young modulus values) increases when going from (911) to (311). Along the  $[0-11]$  direction, the QD-QD distance demonstrates a trend to decreasing, while remaining practically the same along the elastically softer direction  $[-1n0]$  (the smallest Young modulus values). However, again, the above regularities brake down in the case of (311)B substrate due to the largest anisotropy among the investigated orientations.

All of the above mentioned self-assembled QDs become ordered due to the interacting strain fields of successive QD layers and surface diffusion. It is apparent that new possibilities in 3D self-directed QD ordering could be achieved if strain and anisotropic diffusion can be controlled separately. One of the known effective ways to change surface diffusion is the deposition of a few monolayers of another material on a growth surface [80] or a change in the source gas composition [71]. Improvement of InAs QDs optical properties was reported, where  $As_2$  flux was used instead of usual  $As_4$  [81, 82], but differences in physical processes of

lateral and vertical QDs ordering were not under investigation. We use either  $\text{As}_4$  or  $\text{As}_2$  as the arsenic source gas for growth of InGaAs/GaAs QD superlattices to study the role of both surface diffusion and elastic strain in formation and development of 3D ordering of the QDs in a GaAs matrix [83]. In particular, our findings show an influence of As flux type on multilayered growth of (In, Ga)As QDs on GaAs (100). This provides an excellent opportunity to vary and control the symmetry of the diffusion and strain pattern in each layer with the aim to optimize the spatial ordering of nanostructures with identical sizes and shapes in multilayers of QDs.

It is known that, for a given growth conditions, the maximum sticking coefficient is only 0.5 for  $\text{As}_4$ , but it can reach 1.0 for  $\text{As}_2$ . However, for sufficient overpressure of As with the same growth conditions, the sticking coefficient for Ga and In is very readily 1.0 [84]. Therefore, the amount of material grown is completely determined by the group III flux. The use of the  $\text{As}_2$  background for effective manipulation of QD shape, positioning and deformation can be understood by considering surface diffusion. Due to the nature of the  $(2 \times 4)$  GaAs(100) surface reconstruction, the adatoms diffusion length along  $[0-11]$  direction is much larger in comparison with that for  $[011]$  direction.

This anisotropic surface diffusion leads to elongation of the QDs in each layer along the direction of higher mobility. This elongation in turn creates anisotropic strain fields in each capping layer (strain in the  $[0-11]$  direction is smaller than in  $[011]$  [85]), which then enhances the elongation of the QDs subsequently forming chains or wires. The difference between the  $\text{As}_4$  and  $\text{As}_2$  appears to be in terms of limiting the ultimate diffusion lengths. A microprobe-RHEED/SEM study has shown that the lateral flow of Ga atoms is reduced under  $\text{As}_2$  flux in comparison with  $\text{As}_4$  [86]. Since the  $\text{As}_2$  does not need to be cracked in order to incorporate into the crystal [87], having that as the arsenic source provides a lower energy barrier for incorporation and thus a shorter diffusion length for the adatoms [88]. As can be seen from the AFM images of Figs. 25 and 26, it helps to keep the QDs as separate entities forming chains of QDs instead of wires.

Figure 25 shows AFM topographic images of single layers and multilayers for  $x = 0.4$ , which were grown under  $\text{As}_4$  and  $\text{As}_2$  fluxes. QDs in the single layer structures have weak lateral ordering for both  $\text{As}_4$  and  $\text{As}_2$  fluxes (Figs. 25a and b).

However, it is apparent that the sample grown using  $\text{As}_2$  (Fig. 25b) is already more uniform and somewhat more ordered than the one using  $\text{As}_4$  (Fig. 25a), just after the first layer. After further growth, completing the full 15 period structure, well defined periodic dot-chains are observed for both  $\text{As}_4$  and  $\text{As}_2$  growth (Figs. 25c and d). At the same time, it could be seen that the use of either  $\text{As}_4$  or  $\text{As}_2$  during the growth causes significant differences in the density and size of the QDs. These data imply a generally higher surface mobility for QD growth using  $\text{As}_2$  as compared to  $\text{As}_4$ .

The dependence of QD ordering on composition and nominal thickness of deposited wetting layer both for  $\text{As}_4$  and  $\text{As}_2$  fluxes are illustrated in Fig. 26. The same thickness of GaAs spacer layer of 60 MLs was kept in the  $\text{In}_x\text{Ga}_{1-x}\text{As}/\text{GaAs}$

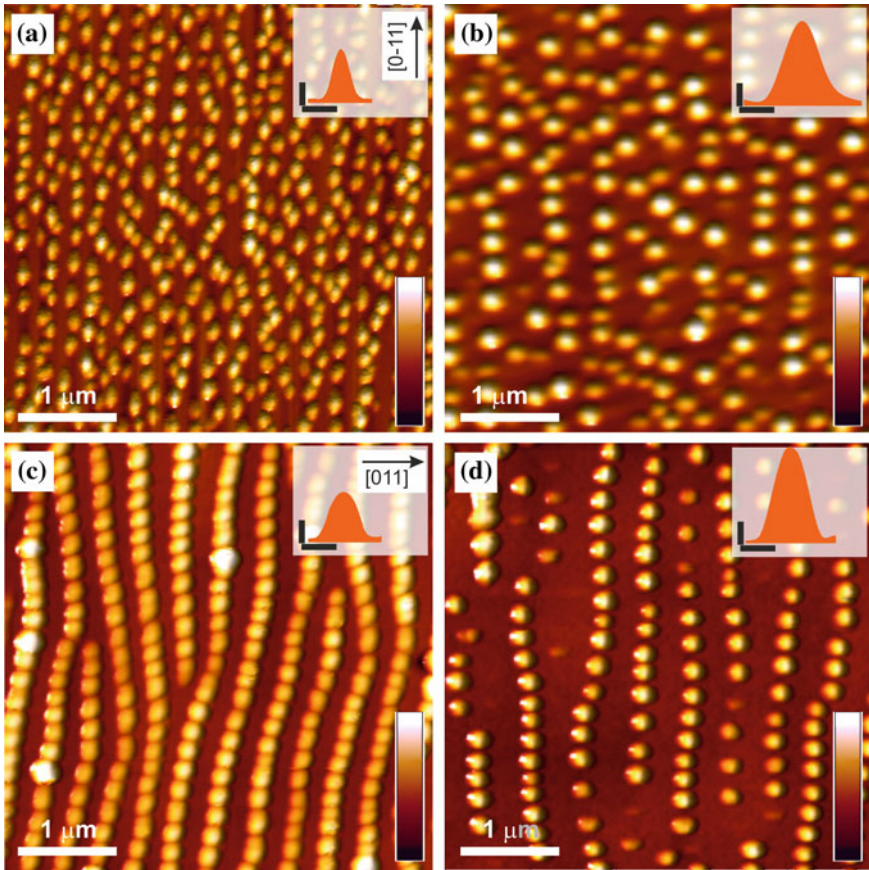


**Fig. 25** AFM images of the In<sub>0.4</sub>Ga<sub>0.6</sub>As QD's on single layer structures ((a), (b)) and 15.5 period structures ((c), (d)) grown using As<sub>4</sub> ((a), (c)) and As<sub>2</sub> ((b), (d)) background fluxes under identical conditions. Insertions in (a)–(d) show the cross-sections (linear profiles) along the [011] direction of most typical QDs determined from size distribution functions (vertical and horizontal scale bars correspond to 6 and 40 nm). Height scale bar corresponds to 15 nm

structures ( $x = 0.3$  for 15.5 MLs and  $x = 0.5$  for 5.7 MLs). For each of these compositions, the dot layers exceed the critical thickness for relaxation by 25 %. As it is seen from Fig. 26, composition increasing from  $x = 0.3$  to 0.5 leads to InGaAs nano-feature transformations from wire-like to closely packed dot-chains in the case of As<sub>4</sub> flux (Figs. 26c and a), and from large elongated QDs to small well separated QDs in the case of As<sub>2</sub> flux (Figs. 26d and b).

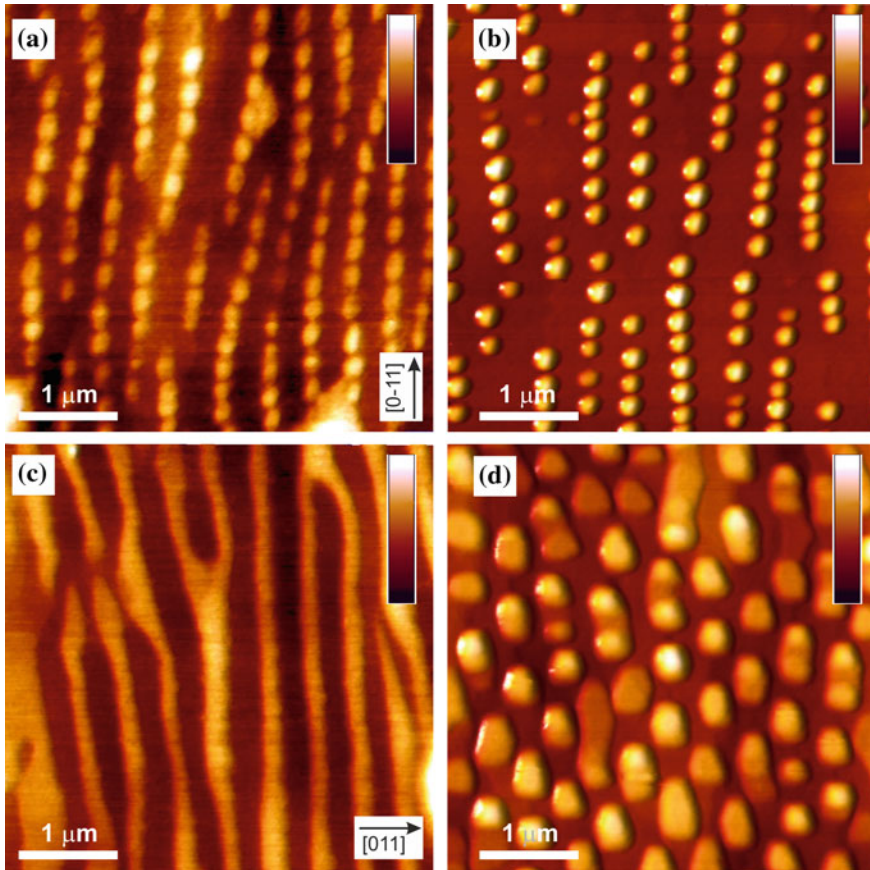


**Fig. 26** AFM images of  $\text{In}_{0.5}\text{Ga}_{0.5}\text{As}$  ((a), (b)) and  $\text{In}_{0.3}\text{Ga}_{0.7}\text{As}$  ((c), (d)) nano-features in multilayered structures grown using  $\text{As}_4$  (left column) and  $\text{As}_2$  (right column) gas fluxes. Height scale bar corresponds to 20 nm

## 4 Conclusion

In conclusion, we tried to describe a common approach to organization of practical AFM diagnostics of surfaces at the sub-micrometer and nano-meter levels. Considerable attention was paid to one of the main AFM applications—topometry of geometrical sizes of surface elements and its metrological traceability. As an example of a system approach to diagnostics of nano-structured surfaces, we adduced our original investigations of growth processes in semiconductor nano-structures with quantum dots. Careful observance of protocols for calibration of AFM as well as tests of uncertainty of measurements added by a shape of the probe tip enabled us to obtain a number of weighty results important for understanding physics of processes of structural ordering in low-dimensional semiconductor systems.

Topometry of surfaces is a most frequently used in practice AFM method with well developed theoretical and metrological foundation. Their description in detail can be found in the list of references. At the same time, these methods are continuously developed, respective facility is upgraded, which enables to considerably enhance their information capability and to widen their application scope.

## References

1. Binnig, G., Rohrer, H.: Scanning tunneling microscope. US Patent 4,343,993, 10 Aug 1982
2. Binnig, G., Rohrer, H., Gerber, C., Weibel, E.: Surface studies by scanning tunneling microscopy. *Phys. Rev. Lett.* **49**(1), 57 (1982)
3. Binnig, G., Rohrer, H., Gerber, C., Weibel, E.:  $7 \times 7$  reconstruction on Si(111) resolved in real space. *Phys. Rev. Lett.* **50**(2), 120 (1983)
4. Young, R.D.: Field emission ultramicrometer. *Rev. Sci. Instrum.* **37**(3), 275 (1966)
5. Young, R., Ward, J., Scire, F.: The topografiner: an instrument for measuring surface microtopography. *Rev. Sci. Instrum.* **43**(7), 999 (1972)
6. Binnig, G., Quate, C.F., Gerber, C.: Atomic force microscope. *Phys. Rev. Lett.* **56**(9), 930 (1986)
7. Binnig, G.K.: Atomic force microscope and method for imaging surfaces with atomic resolution. US Patent 33,387, 16 Oct 1990
8. Belaidi, S., Girard, P., Leveque, G.: Electrostatic forces acting on the tip in atomic force microscopy: modelization and comparison with analytic expressions. *J. Appl. Phys.* **81**(3), 1023 (1997)
9. Martin, Y., Abraham, D.W., Wickramasinghe, H.K.: High-resolution capacitance measurement and potentiometry by force microscopy. *Appl. Phys. Lett.* **52**(13), 1103 (1988)
10. Nonnenmacher, M., o'Boyle, M., Wickramasinghe, H.: Kelvin probe force microscopy. *Appl. Phys. Lett.* **58**, 2921 (1991)
11. Jacobs, H., Leuchtmann, P., Homan, O., Stemmer, A.: Resolution and contrast in Kelvin probe force microscopy. *J. Appl. Phys.* **84**(3), 1168 (1998)
12. Martin, Y., Wickramasinghe, H.K.: Magnetic imaging by "force microscopy" with 1000 Å resolution. *Appl. Phys. Lett.* **50**(20), 1455 (1987)
13. Gröning, O., Küttel, O., Gröning, P., Schlapbach, L.: Field emission from DLC films. *Appl. Surf. Sci.* **111**, 135 (1997)
14. Zhang, L., Sakai, T., Sakuma, N., Ono, T., Nakayama, K.: Nanostructural conductivity and surface-potential study of low-field-emission carbon films with conductive scanning probe microscopy. *Appl. Phys. Lett.* **75**(22), 3527 (1999)
15. De Wolf, P., Clarysse, T., Vandervorst, W., Hellemans, L., Niedermann, P., Hanni, W.: Cross-sectional nano-spreading resistance profiling. *J. Vac. Sci. Technol., B* **16**(1), 355 (1998)
16. Williams, C.C., Slinkman, J., Hough, W.P., Wickramasinghe, H.K.: Lateral dopant profiling with 200 nm resolution by scanning capacitance microscopy. *Appl. Phys. Lett.* **55**(16), 1662 (1989)
17. Baño, A.M., Reifenberger, R.G. (ed.): Atomic force microscopy in liquid. Biological applications. Wiley, Germany, 2012
18. Noy, A. (ed.): Handbook of molecular force spectroscopy. Springer, New York, 2008
19. Bhushan, B. (ed.) Nanotribology and nanomechanics: an introduction. Springer, Heidelberg, 2008
20. Foster, A., Hofer, W.A.: Scanning probe microscopy–atomic scale engineering by forces and currents. Springer, Heidelberg, 2006

21. Kalinin, S.V., Gruverman, A. (ed.): Scanning probe microscopy (2 vol. set): electrical and electromechanical phenomena at the nanoscale. Springer, New York, 2007
22. Kalinin, S.V., Gruverman, A. (ed.): Scanning probe microscopy of functional materials: nanoscale imaging and spectroscopy. Springer, New York, 2011
23. Samor, P. (ed.) Scanning probe microscopies beyond imaging: manipulation of molecules and nanostructures. Wiley, Germany, 2006
24. Landis, S. (ed.) Nano-lithography (Wiley-ISTE, New York, 2011)
25. Israelachvili, N.: Intermolecular and surface forces, 3rd ed. (Academic Press, New York, 2011)
26. Butt, H.-J., Cappella, B., Kappl, M.: Force measurements with the atomic force microscope: technique, interpretation and applications. *Surf. Sci. Rep.* **59**(1), 1 (2005)
27. Cappella, B., Dietler, G.: Force-distance curves by atomic force microscopy. *Surf. Sci. Rep.* **34**(1), 1 (1999)
28. Rabe, U., Janser, K., Arnold, W.: Vibrations of free and surface-coupled atomic force microscope cantilevers: theory and experiment. *Rev. Sci. Instrum.* **67**(9), 3281 (1996)
29. García, R., Pérezb, R.: Dynamic atomic force microscopy methods. *Surf. Sci. Rep.* **47**(6–8), 197 (2002)
30. Whitehouse, D.J: Handbook of surface and nanometrology. CRC Press, Boca Raton, 2010
31. Gao, W.: Precision nanometrology: sensors and measuring systems for nanomanufacturing. (Springer, London, 2010)
32. Leach, R.: Fundamental principles of engineering nanometrology. William Andrew, Amsterdam, 2009
33. Klapetek, P. (ed.): Quantitative data processing in scanning probe microscopy: SPM applications for nanometrology (micro and nano technologies). William Andrew, Norwich, 2013
34. ISO/TC 201/SC 9 - Scanning probe microscopy. International organization for standardization, 2013, [http://isostore.sii.org.il/sii/home/catalogue\\_tc/catalogue\\_tc\\_browse.htm?commid=354756](http://isostore.sii.org.il/sii/home/catalogue_tc/catalogue_tc_browse.htm?commid=354756). Accessed 22 Nov 2013
35. ISO/DIS 13083. Standards on the definition and calibration of spatial resolution of scanning spreading resistance microscopy and scanning capacitance microscopy. International organization for standardization, 2013. [http://isostore.sii.org.il/sii/home/catalogue\\_tc/catalogue\\_detail.htm?csnumber=52691](http://isostore.sii.org.il/sii/home/catalogue_tc/catalogue_detail.htm?csnumber=52691). Accessed 22 Nov 2013
36. International Organization for Standardization: Geometrical product specifications - Surface texture: Areal - Part 2: Terms, definitions and surface texture parameters, (ISO 25178-2:2012) (2012 )
37. ASME Intl., Surface Texture (Surface Roughness, Waviness, and Lay) ASME B46.1 (2009)
38. Dowling, A., Clift, R., Grobert, N., Hutton, D., Oliver, R., O'neil, O., Pethica, J., Pidgeon, N., Porritt, J., Ryan, J.: Nanoscience and nanotechnologies: opportunities and uncertainties. London: The royal society and The royal academy of engineering report, 61 (2004)
39. Wilkening, G., Koenders, L.: Nanoscale calibration standards and methods: dimensional and related measurements in the micro and nanometer range. Wiley, Weinheim, 2005
40. Lytvyn, O.S., Lytvyn, P.M., Prokopenko, I.V., Sheremeta, T.I.: Peculiarities of nanostructures topometry studied by atomic force microscopy methods. *Nanosyst. Nanomater. Nanotechnol.* **6**(1), 33 (2008)
41. Ferreira, S.O., Neves, B.R.A., Magalhães-Paniago, R., Malachias, A., Rappl, P.H.d.O, Ueta, A., Abramof, E., Andrade, M.S.: AFM characterization of PbTe quantum dots grown by molecular beam epitaxy under Volmer–Weber mode. *J. Cryst. Growth* **231**(1), 121 (2001)
42. Minhua, Z., Vaneet, S., Haoyan, W., Robert, R.B., Jeffrey, A.S., Fotios, P., Bryan, D.H.: Ultrasharp and high aspect ratio carbon nanotube atomic force microscopy probes for enhanced surface potential imaging. *Nanotechnology* **19**(23), 235704 (2008)
43. Tay, A.B.H., Thong, J.T.L.: High-resolution nanowire atomic force microscope probe grownby a field-emission induced process. *Appl. Phys. Lett.* **84**(25), 5207 (2004)
44. Givargizov, E., Stepanova, A., Obolenskaya, L., Mashkova, E., Molchanov, V., Givargizov ME., Rangelow, I.: Whisker probes. *Ultramicroscopy* **82**(1), 57 (2000)

45. Keller, D.: Reconstruction of STM and AFM images distorted by finite-size tips. *Surf. Sci.* **253**(1), 353 (1991)
46. Bonnet, N., Dongmo, S., Vautrot, P., Troyon, M.: A mathematical morphology approach to image formation and image restoration in scanning tunnelling and atomic force microscopies. *Microsc. Microanal. Microstruct.* **5**(4–6), 477 (1994)
47. Markiewicz, P., Goh, M.C.: Atomic force microscope tip deconvolution using calibration arrays. *Rev. Sci. Instrum.* **66**(5), 3186 (1995)
48. Hübner, U., Morgenroth, W., Meyer, H.G., Sulzbach, T., Brendel, B., Mirandé, W.: Downwards to metrology in nanoscale: determination of the AFM tip shape with well-known sharp-edged calibration structures. *Appl. Phys. A* **76**(6), 913 (2003)
49. Villarrubia, J.S.: Algorithm for scanned probe microscope image simulation, surface reconstruction, and tip estimation. *J. Res. Natl. Inst. Stan. Technol.* **102**, 425 (1997)
50. Dongmo, L.S., Villarrubia, J.S., Jones, S.N., Renegar, T.B., Postek, M.T., Song, J.F.: Experimental test of blind tip reconstruction for scanning probe microscopy. *Ultramicroscopy* **85**(3), 141 (2000)
51. Tranchida, D., Piccarolo, S., Deblieck, R.: Some experimental issues of AFM tip blind estimation: the effect of noise and resolution. *Meas. Sci. Technol.* **17**(10), 2630 (2006)
52. Castle, J., Zhdan, P.: Characterization of surface topography by SEM and SFM: problems and solutions. *J. Phys. D Appl. Phys.* **30**(5), 722 (1997)
53. Krasil'nik, Z.F., Lytvyn, P., Lobanov, D.N., Mestres, N., Novikov, A.V., Pascual, J., Valakh, M.Y., Yukhymchuk, V.A.: Microscopic and optical investigation of Ge nanoislands on silicon substrates. *Nanotechnology* **13**(1), 81 (2002)
54. Shchukin, V.A., Ledentsov, N.N., Kop'ev, P.S., Bimberg, D.: Spontaneous ordering of arrays of coherent strained Islands. *Phys. Rev. Lett.* **75**(16), 2968 (1995)
55. Ross, F.M., Tersoff, J., Tromp, R.M.: Coarsening of self-assembled Ge quantum dots on Si(001). *Phys. Rev. Lett.* **80**(5), 984 (1998)
56. Krasil'nik, Z.F., Dolgov, I.V., Drozdov, Y.N., Filatov, D.O., Gusev, S.A., Lobanov, D.N., Moldavskaya, L.D., Novikov, A.V., Postnikov, V.V., Vostokov, N.V.: The elastic strain and composition of self-assembled GeSi islands on Si (001). *Thin Solid Films* **367**(1), 171 (2000)
57. Valakh, M.Y., Lytvyn, P.M., Nikolenko, A.S., Strelchuk, V.V., Krasilnik, Z.F., Lobanov, D.N., Novikov, A.V.: Gigantic uphill diffusion during self-assembled growth of Ge quantum dots on strained SiGe sublayers. *Appl. Phys. Lett.* **96**(14), 141909 (2010)
58. Strelchuk, V.V., Nikolenko, A.S., Lytvyn, P.M., Kladko, V.P., Gudymenko, A.I., Valakh, M.Y., Krasilnik, Z.F., Lobanov, D.N., Novikov, A.V.: Effects of the lateral ordering of self-assembled SiGe nanoislands grown on strained  $\text{Si}_{1-x}\text{Ge}_x$  buffer layers. *Semiconductors* **46**(5), 647 (2012)
59. Lobanov, D.N., Novikov, A.V., Vostokov, N.V., Drozdov, Y.N., Yablonskiy, A.N., Krasilnik, Z.F., Stoffel, M., Denker, U., Schmidt, O.G.: Growth and photoluminescence of self-assembled islands obtained during the deposition of Ge on a strained SiGe layer. *Opt. Mater.* **27**(5), 818 (2005)
60. Vostokov, N.V., Drozdov, Y.N., Krasil'nik, Z.F., Kuznetsov, O.A., Novikov, A.V., Perevoshchikov, V.A., Shaleev, M.V.:  $\text{Si}_{1-x}\text{Ge}_x/\text{Si}$  (001) relaxed buffer layers grown by chemical vapor deposition at atmospheric pressure. *Phys. Solid State* **47**(1), 42 (2005)
61. Geguzin, Y.E.: Ascending diffusion and the diffusion aftereffect. *Sov. Phys. Uspekhi* **29**(5), 467 (1986)
62. Fafard, S., Hinzer, K., Raymond, S., Dion, M., McCaffrey, J., Feng, Y., Charbonneau, S.: Red-emitting semiconductor quantum dot lasers. *Science* **274**(5291), 1350 (1996)
63. Jin, C.Y., Liu, H.Y., Groom, K.M., Jiang, Q., Hopkinson, M., Badcock, T.J., Royce, R.J., Mowbray, D.J.: Effects of photon and thermal coupling mechanisms on the characteristics of self-assembled InAs/GaAs quantum dot lasers. *Phys. Rev. B* **76**(8), 085315 (2007)
64. Liu, H.C., Gao, M., McCaffrey, J., Wasilewski, Z.R., Fafard, S.: Quantum dot infrared photodetectors. *Appl. Phys. Lett.* **78**(1), 79 (2001)

65. Maimon, S., Finkman, E., Bahir, G., Schacham, S.E., Garcia, J.M., Petroff, P.M.: Intersublevel transitions in InAs/GaAs quantum dots infrared photodetectors. *Appl. Phys. Lett.* **73**(14), 2003 (1998)
66. Ye, Z., Campbell, J.C., Chen, Z., Kim, E.-T., Madhukar, A.: Voltage-controllable multiwavelength InAs quantum-dot infrared photodetectors for mid- and far-infrared detection. *J. Appl. Phys.* **92**(7), 4141 (2002)
67. Schmidbauer, M., Wang, Z.M., Mazur, Y.I., Lytvyn, P.M., Salamo, G.J., Grigoriev, D., Schafer, P., Kohler, R., Hanke, M.: Initial stages of chain formation in a single layer of (In, Ga) As quantum dots grown on GaAs (100). *Appl. Phys. Lett.* **91**(9), 093110 (2007)
68. Hanke, M., Dubsclaff, M., Schmidbauer, M., Wang, Z.M., Mazur, Y.I., Lytvyn, P.M., Lee, J.H., Salamo, G.J.: On the complex behavior of strain relaxation in (In, Ga) As/GaAs (001) quantum dot molecules. *Appl. Phys. Lett.* **95**(2), 023103 (2009)
69. Mehta, S.K., Muralidharan, R., Sharda, G.D., Jain, R.K.: Some investigations on oval defects in MBE-grown GaAs. *Semicond. Sci. Technol.* **7**(5), 635 (1992)
70. Lytvyn, P.M., Prokopenko, I.V., Strelchuk, V.V., Mazur, Y.I., Wang, Z.M., Salamo, G.J.: Microsize defects in InGaAs/GaAs (N11) A/B multilayers quantum dot stacks. *J. Cryst. Growth* **284**(1), 47 (2005)
71. Itoh, M.: Atomic-scale homoepitaxial growth simulations of reconstructed III-V surfaces. *Prog. Surf. Sci.* **66**(3), 53 (2001)
72. Apostolopoulos, G., Herfort, J., Däweritz, L., Ploog, K.H., Luysberg, M.: Reentrant mound formation in GaAs(001) homoepitaxy observed by ex situ atomic force microscopy. *Phys. Rev. Lett.* **84**(15), 3358 (2000)
73. Wang, Z.M., Mazur, Y.I., Salamo, G.J., Lytvyn, P.M., Strelchuk, V.V., Valakh, M.Y.: Persistence of (In, Ga) As quantum-dot chains under index deviation from GaAs (100). *Appl. Phys. Lett.* **84**(23), 4681 (2004)
74. Wang, Z.M., Seydmohamadi, S., Lee, J.H., Salamo, G.J.: Surface ordering of (In, Ga)As quantum dots controlled by GaAs substrate indexes. *Appl. Phys. Lett.* **85**(21), 5031 (2004)
75. Wang, X.D., Liu, N., Shih, C.K., Govindaraju, S., Holmes, A.L.: Spatial correlation-anticorrelation in strain-driven self-assembled InGaAs quantum dots. *Appl. Phys. Lett.* **85**(8), 1356 (2004)
76. Strassburg, M., Kutzer, V., Pohl, U.W., Hoffmann, A., Broser, I., Ledentsov, N.N., Bimberg, D., Rosenauer, A., Fischer, U., Gerthsen, D., Krestnikov, I.L., Maximov, M.V., Kop'ev, P.S., Alferov, Z.I.: Gain studies of (Cd, Zn)Se quantum islands in a ZnSe matrix. *Appl. Phys. Lett.* **72**(8), 942 (1998)
77. Shchukin, V.A., Bimberg, D., Malyshev, V.G., Ledentsov, N.N.: Vertical correlations and anticorrelations in multisheet arrays of two-dimensional islands. *Phys. Rev. B* **57**(19), 12262 (1998)
78. Lytvyn, P.M., Strelchuk, V.V., Kolomys, O.F., Prokopenko, I.V., Valakh, M.Y., Mazur, Y.I., Wang, Z.M., Salamo, G.J., Hanke, M.: Two-dimensional ordering of (In, Ga)As quantum dots in vertical multilayers grown on GaAs(100) and (n11). *Appl. Phys. Lett.* **91**(17), 173118 (2007)
79. Sirotnin, Y.I., Shaalkokoya, M.P.: *Fundamentals of crystal physics*. MIR Publishers, Moscow, 1982
80. Cirlin, G.E., Tonkikh, A.A., Ptitsyn, V.E., Dubrovskii, V.G., Masalov, S.A., Evtikhiev, V.P., Denisov, D.V., Ustinov, V.M., Werner, P.: Influence of antimony on the morphology and properties of an array of Ge/Si (100) quantum dots. *Phys. Solid State* **47**(1), 58 (2005)
81. Sugaya, T., Amano, T., Komori, K.: Improved optical properties of InAs quantum dots grown with an As<sub>2</sub> source using molecular beam epitaxy. *J. Appl. Phys.* **100**(6), 063107 (2006)
82. Sugaya, T., Numakami, O., Oshima, R., Furue, S., Komaki, H., Amano, T., Matsubara, K., Okano, Y., Niki, S.: Ultra-high stacks of InGaAs/GaAs quantum dots for high efficiency solar cells. *Energy Environ. Sci.* **5**(3), 6233 (2012)
83. Lytvyn, P.M., Mazur, Y.I., Marega Jr, E., Dorogan, V.G., Kladko, V.P., Slobodian, M.V., Strelchuk, V.V., Hussein, M.L., Ware, M.E., Salamo, G.J.: *Engineering of 3D self-directed*



- quantum dot ordering in multilayer InGaAs/GaAs nanostructures by means of flux gas composition. *Nanotechnology* **19**(50), 505605 (2008)
84. Kaldis, E. (ed.): *Current topics in materials science* (Elsevier Science Ltd, New York, 1981)
  85. Wang, Z.M., Holmes, K., Mazur, Y.I., Salamo, G.J.: Fabrication of (In, Ga)As quantum-dot chains on GaAs(100). *Appl. Phys. Lett.* **84**(11), 1931 (2004)
  86. Ogura, T., Kishimoto, D., Nishinaga, T.: Effect of As molecular species on inter-surface diffusion in GaAs MBE for ridge structure fabrication. *J. Cryst. Growth* **226**(2), 179 (2001)
  87. Morgan, C.G., Kratzer, P., Scheffler, M.: Arsenic dimer dynamics during MBE growth: theoretical evidence for a novel chemisorption state of As<sub>2</sub> molecules on GaAs surfaces. *Phys. Rev. Lett.* **82**(24), 4886 (1999)
  88. Sugaya, T., Komori, K., Yamauchi, S., Amano, T.: 1.3 μm InAs quantum dots grown with an As<sub>2</sub> source using molecular-beam epitaxy. *J. Vac. Sci. Technol., B* **23**(3), 1243 (2005)